



Originally published as:

León Soto, G., Sandvol, E., Ni, J. F., Flesch, L., Hearn, T. M., Tilmann, F., Chen, J., Brown, L. D. (2012): Significant and vertically coherent seismic anisotropy beneath eastern Tibet. - *Journal of Geophysical Research*, 117, B05308

DOI: [10.1029/2011JB008919](https://doi.org/10.1029/2011JB008919)

Significant and vertically coherent seismic anisotropy beneath eastern Tibet

Gerardo León Soto,^{1,2} Eric Sandvol,³ James F. Ni,¹ Lucy Flesch,⁴ Thomas M. Hearn,¹ Frederik Tilmann,^{5,6} John Chen,⁷ and Larry D. Brown⁸

Received 5 October 2011; revised 28 March 2012; accepted 30 March 2012; published 18 May 2012.

[1] Shear wave splitting measurements using teleseismic SKS and SKKS phases recorded by the INDEPTH-IV arrays has revealed a strong upper mantle anisotropic fabric in northeastern Tibet with large delay times of up to 2.2 s, suggesting that anisotropy exists in both the lithospheric and asthenospheric mantle. The coherence among fast polarization orientations of split core phases and the left-lateral slip on eastern-striking, southern-striking faults in eastern Tibet and the surface deformation fields calculated from both GPS observations and Quaternary fault slip rates support the idea that left-lateral shear strain is the predominant cause of the orientation of the upper mantle petrofabrics. We suggest the bending of the Eastern Himalayan Syntaxis around the foundering Burma-Andaman-Sumatra slab also contributes to the observed seismic anisotropy in the Eastern Himalayan Syntaxis region. Two plausible competing processes are proposed for the flow of asthenosphere in eastern Tibet. In the first, the deforming lithosphere glides over the passive asthenosphere inducing flow in the asthenospheric mantle. In the second, the asthenosphere beneath northeastern Tibet is squeezed between the advancing Indian continental lithosphere and the thick Tarim and Qaidam lithospheric blocks to the north. A westward retreat of the Burma slab from Eurasia may induce flow that is toroidal and located exclusively around the northern edge of the slab. The rotation of fast orientations for stations in the Eastern Himalayan Syntaxis region are consistent with the toroidal flow pattern as well as the rotational deformation of the overlying lithosphere.

Citation: León Soto, G., E. Sandvol, J. F. Ni, L. Flesch, T. M. Hearn, F. Tilmann, J. Chen, and L. D. Brown (2012), Significant and vertically coherent seismic anisotropy beneath eastern Tibet, *J. Geophys. Res.*, 117, B05308, doi:10.1029/2011JB008919.

1. Introduction

[2] Over the past two decades, a large number of geophysical studies have targeted the architecture and dynamics of the Tibetan Plateau with the intention of characterizing the ongoing continental deformation processes. Global Position

System (GPS) measurements document a gradual change of surface motion from northward in southern Tibet to a clockwise rotation motion around the Eastern Himalayan Syntaxis with respect to stable Eurasia [Zhang *et al.*, 2004]. This motion of crustal material continues south to latitude 27°N where the velocity vector with respect to stable Eurasia turns west toward Burma. Since GPS measurements, faulting, as well as focal mechanisms all indicate the southern Yunnan and northern Burma (adjacent to China) is under E-W extension, this change in direction of the velocity vector may be a consequence of the E-W extension of the Panxi rift (in Yunnan province), where abundant north-south trending normal faults occur with recent bi-modal volcanism. The Panxi rift is located in the Burma back arc and is a result of lithospheric extension thought to be induced by corner-flow (poloidal flow) associated with the rollback of the subducted Burma slab [e.g., Ni *et al.*, 1989].

[3] In addition to the convergence taken up at the plateau margins, two extreme and opposite views of the mechanisms responsible for the shortening and plateau uplift are: 1) deformation is essentially continuous and can be approximated by a viscous thin sheet [e.g., England and Houseman, 1986; England and Molnar, 1997]; and 2) discrete tectonic blocks, with little internal deformation, are being extruded eastward between large lithospheric-scale strike-slip faults

¹Department of Physics, New Mexico State University, Las Cruces, New Mexico, USA.

²Now at Departamento de Geología y Mineralogía, Universidad Michoacana de San Nicolás de Hidalgo, Morelia, Mexico.

³Department of Geological Sciences, University of Missouri, Columbia, Missouri, USA.

⁴Department of Earth and Atmospheric Sciences, Purdue University, West Lafayette, Indiana, USA.

⁵Bullard Laboratories, Department of Earth Sciences, University of Cambridge, Cambridge, UK.

⁶Now at Sektion 2.4, Seismologie, Helmholtz-Zentrum Potsdam, Deutsches GeoForschungsZentrum, Potsdam, Germany.

⁷Institute of Theoretical and Applied Geophysics, School of Earth and Space Sciences, Peking University, Beijing, China.

⁸Department of Earth and Atmospheric Sciences, Cornell University, Ithaca, New York, USA.

Corresponding author: G. León Soto, Departamento de Geología y Mineralogía, Universidad Michoacana de San Nicolás de Hidalgo, Morelia 58060, Mexico. (gleon.soto@gmail.com)

[e.g., *Tapponnier et al.*, 1982, 2001]. Abundant GPS data from eastern Tibet [*Zhang et al.*, 2004], seem to show, in our opinion, that a model of rigid blocks separated by narrow fault zones along which upper crustal deformation is completely localized seems more plausible than a model with continuous deformation.

[4] Although GPS studies yield good estimates of the surface velocity, the deformation of lithospheric and asthenospheric mantle at depth is less clear. The upper mantle beneath the Tibetan plateau deforms as the north-advancing Indian plate is compressing the Tibetan lithosphere. Asthenosphere beneath eastern Tibet is also flowing in response to the motions of upper mantle in central Tibet and eastern China. Deformation of the upper mantle preferentially aligns minerals within rocks [e.g., *Kumazawa and Anderson*, 1969; *Babuska and Kara*, 1991] and this alignment causes elastic anisotropy, which affects how seismic waves propagate in different directions or polarizations.

[5] Transverse anisotropic models, assuming a single homogeneous layer with a horizontal axis of symmetry, have previously been produced from analyses of shear wave splitting to explain mantle deformation for the central and eastern Tibetan plateau and the Himalayas [e.g., *McNamara et al.*, 1994; *Herquel et al.*, 1995; *Hirn et al.*, 1995; *Lavé et al.*, 1996; *Sandvol et al.*, 1997; *Huang et al.*, 2000; *Lev et al.*, 2006; *Sol et al.*, 2007; *Fu et al.*, 2008; *Wang et al.*, 2008; *Chen et al.*, 2010]. No coherent shear wave splitting has been observed in the southern Lhasa terrane [e.g., *Hirn et al.*, 1995; *Sandvol et al.*, 1997; *Huang et al.*, 2000; *Fu et al.*, 2008; *Chen et al.*, 2010] or beneath the Himalayas where the underthrusting Indian continental lithosphere is below the upper crust. The lack of significant and coherent azimuthal anisotropy could be attributed to a two-layer anisotropy with near perpendicular symmetry axes [*Gao and Liu*, 2009] or the lack of coherent anisotropy of the underthrusting Indian shield [*Sandvol et al.*, 1997; *Chen and Özalaybey*, 1998; *Fu et al.*, 2008; *Chen et al.*, 2010].

[6] In central and northern Tibet *McNamara et al.* [1994] found a systematic rotation of the fast azimuth from about 45° (NE) to 90° (E-W) from south to north along the Golmud-Lhasa highway. In most cases, the fast polarization orientations appear to be parallel to surface geologic features and well explained by single layer transverse anisotropy with a horizontal symmetry axis [*Holt*, 2000; *Huang et al.*, 2000; *Lev et al.*, 2006; *Sol et al.*, 2007; *Chen et al.*, 2010]. A dramatic variation in delay times for closely spaced stations crossing the Kunlun fault was also observed. A previously identified zone of inefficient Sn propagation [e.g., *Ni and Barazangi*, 1983] correlates well with the region of large splitting in northern Tibet suggesting that the same underlying tectonic process affected both. Taken in conjunction with decades of geophysical observations in Tibet, the anisotropic measurements in central northern Tibet (north of ~33°N and south of the Kunlun Mountains) with predominately E-W fast polarization are consistent with a model where hot upper mantle beneath the crust is being squeezed and sheared between the advancing Indian lithosphere to the south and the Tarim and Qaidam lithosphere to the north [*Davis et al.*, 1997; *Huang et al.*, 2000; *Chen et al.*, 2010].

[7] In southeastern Tibet, the majority of the fast polarization orientations revealed a pronounced transition from E-W in the Eastern Himalayan Syntaxis to N-S in Sichuan

province that is approximately parallel to the surficial geology including major sutures and shear-zones and the surface velocity field derived from GPS data [*Sol et al.*, 2007; *Lev et al.*, 2006; *Wang et al.*, 2008]. For most of eastern Tibet, shear wave splitting measurements appear consistent with a vertically coherent deformation of the lithospheric mantle where the deformation regime apparently changes from simple shear on the plateau to pure shear in its off-plateau margins [*Wang et al.*, 2008]. In this study we present new and extensive shear wave splitting measurements from the INDEPTH-IV seismic array (in northeastern Tibet) and combine them with the existing shear wave splitting parameters of the entire eastern Tibet to address the kinematics and dynamics of the Tibetan plateau.

2. Tectonic Background

[8] The Tibetan Plateau sits at an average elevation of over 5 km and is the result of continental collision between the Indian and Eurasian plates, which started about 50–55 Ma [e.g., *Garzanti and Van Haver*, 1988; *Yin and Harrison*, 2000; *Rowley and Currie*, 2006; *Royden et al.*, 2008; *Najman et al.*, 2010] (Figure 1). The dynamic process that formed the central Tibetan Plateau is mainly related to underthrusting of the Indian continental lithosphere beneath southern Eurasia [*Argand*, 1924; *Ni and Barazangi*, 1984; *Nelson et al.*, 1996; *Mattauer et al.*, 1999; *Tilmann et al.*, 2003; *Li et al.*, 2008]. In central Tibet (80°E to ~92°E), the Indian continental lithosphere underthrusts and thickens the crust of southern Tibet to ~75–85 km creating the majestic mountain ranges of the Himalayas and Karakorum [*Zhao et al.*, 1993; *Nelson et al.*, 1996; *Kind et al.*, 1996; *Kumar et al.*, 2006; *Nábělek et al.*, 2009; *Tseng et al.*, 2009]. In contrast, the lithosphere of northern Tibet is composed of thickened accreted terranes [e.g., *Tilmann et al.*, 2003; *McKenzie and Priestley*, 2008]. How far the underthrusting Indian continental lithosphere extends northward greatly affects the regional tectonics of the plateau. Correlation of seismic anisotropy and interpretations of Bouguer gravity anomalies in Tibet indicates that, in central Tibet, Indian mantle lithosphere extends northward to near 33°N [*Chen and Özalaybey*, 1998; *Chen et al.*, 2010]. Recent research using tomographic images and receiver functions found that to the west (~81°E), where the plateau is narrower in the N-S direction, the Indian lithosphere reaches the Jinsha-River Suture [*Zhao et al.*, 2010], while in the east the Indian continental lithosphere (~90°E) terminates just north of the Indus-Yalong Suture [*Li et al.*, 2008; *Zhao et al.*, 2010] (Figure 1). The eastern edge of the continental Indian lithosphere appears to occur somewhere in the Eastern Himalayan Syntaxis (92°–94°E) where the surface morphology changes from N-S oriented rift valleys to a curved strike-slip faults.

[9] Much of the active deformation of the eastern plateau is characterized by strike-slip faulting (Figure 1). Displacement on these strike-slip faults may allow lateral transport of materials, known as “extrusion,” or “continental escape,” with the convergence of the India and Eurasia plates [*Tapponnier and Molnar*, 1977]. *England and Molnar* [1990] suggested that extrusion is merely an illusion, and that instead the left-lateral slip on east-striking faults in eastern Tibet is a manifestation of north-striking right-lateral simple shear. They estimated that the east-striking left lateral

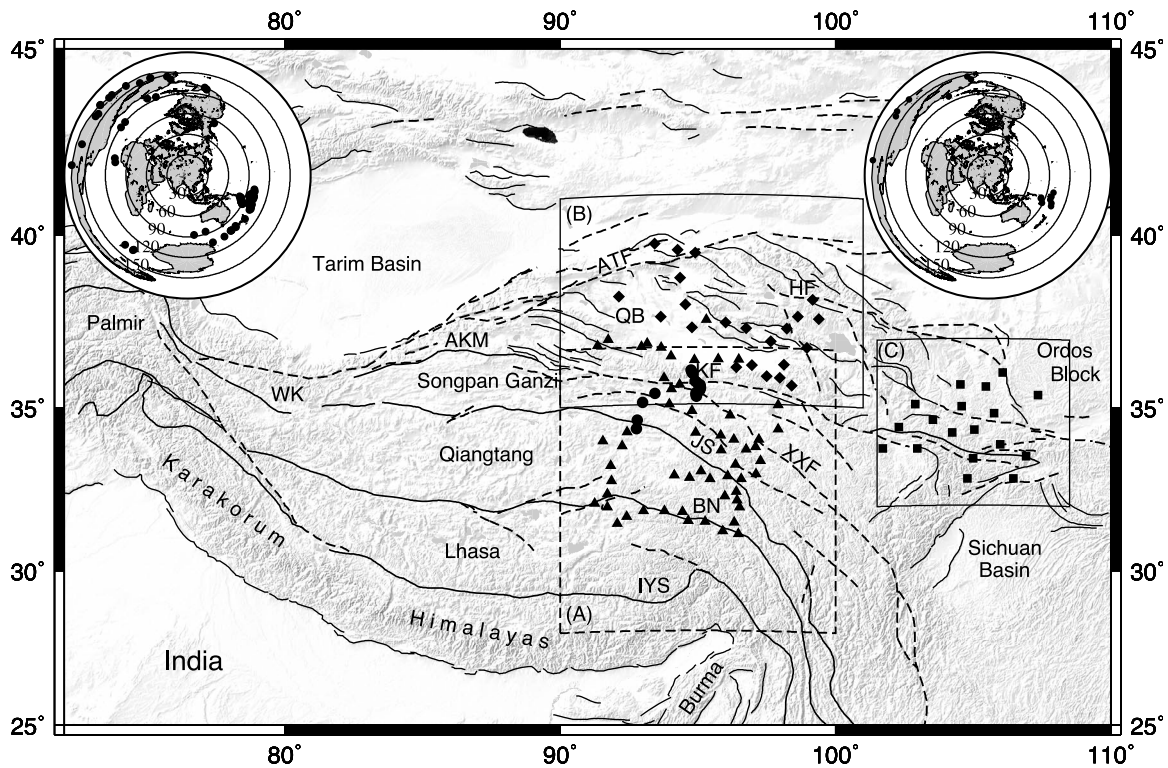


Figure 1. Topography and major tectonic features map of the Tibetan Plateau and surrounding regions. Stations of the INDEPTH-IV linear array are shown as black circles. Stations from the 2-D array are shown by triangles. Stations from the 18-station northeastern Tibet array are shown as black squares. Stations in the Qaidam basin and Qilian Shan are shown as black diamonds. Thick black lines stand for the suture zones, dashed black lines are strike-slip faults, and thin black lines are thrust faults. Blocks A, B, and C represent regions of the three deployments that are discussed in Figures 8–10. The top left inset displays events recorded by the 2-D array SKS and the top right inset displays events for the 1-D array. The Burma subduction zone begins at the southeastern termination of the Eastern Himalayan Syntaxis and the northern edge of the Burma slab is near 27°N . Abbreviation of geological and tectonic structures are: IYS, Indus Yalug suture; BN, Banggong-Nujiang suture; JS, Jinsha suture; QB, Qaidam Basin; AKM, Ayimaqin Kunlun Mutztagh suture; KF, Kunlun fault, ATF, Altyn Tagh fault; HF, Haiyuan fault; XXF, Xiangshuie-Xiaojiang fault; WK, Western Kunlun mountains.

faults and the crustal blocks are rotating clockwise at $1\text{--}2^{\circ}\text{ Myr}^{-1}$, the east-west dimension of eastern Tibet is being lengthened at $10\text{--}20\text{ mm yr}^{-1}$, and little material is moving eastward into Eurasia by sinistral slip on major faults in eastern Tibet.

[10] The central eastern Tibetan plateau lacks any evidence for large-scale young crustal shortening since Mesozoic time [e.g., Royden *et al.*, 1997]. This observation led Royden *et al.* [1997] to conclude that surface deformation in eastern Tibet is strongly decoupled from motion of the lower crust and the net crustal thickening is mainly due to lower crustal flow. Further understanding of the depth-dependent rheology, the thickening process, and the relationship between lower crustal flow and the growth of the northern and eastern Tibetan plateau remain challenging issues [e.g., Royden *et al.*, 2008; Karplus *et al.*, 2011].

[11] In spite of being a collision setting, thrust faulting in Tibet is mainly concentrated in the Himalayas, the northernmost part of the plateau bordering Qaidam basin and the Qiliang Shan, and along the eastern margin of Tibet (Figure 1). Other factors, such as gravitational potential energy variations associated with the high topography and

the boundary condition that India applies to Eurasia have been considered as the main causes of deformation of the Tibetan plateau and adjacent regions [England and Houseman, 1989; Flesch *et al.*, 2001]. Deviatoric stresses induce an E-W extension on the southern Tibetan plateau [McCaffrey and Nábělek, 1998] and compression generates left-lateral strike-slip faulting in central eastern and northeastern Tibetan Plateau. The Kunlun fault is one of the largest examples of strike-slip motion in Tibet. It bounds northern Tibet, has a slip rate of $10 \pm 1\text{ mm/yr}$, and has been active for the last 7 Ma [Van der Woerd *et al.*, 1998; Cowgill, 2007]. The relative uniform high topographical relief of the Tibetan Plateau abruptly lowers to the north of the Kunlun fault, dropping about 2 km in Qaidam basin.

3. Data

[12] Data used in this study were collected by the INDEPTH-IV 2-D and linear arrays (Figure 1). The linear array (stations shown as black circles) utilized equipment from the UK and German consortium and was recorded for one year (May 30, 2007 to September 6, 2008) at a sampling

rate of 50 sps. All temporary seismic stations from the 2-D array were equipped with broadband sensors and were recorded with a sampling rate of 25 sps. The average spacing between stations is less than 100 km, although in some areas the stations were less sparsely distributed. The INDEPTH-IV 2-D array, consisting of 98 PASSCAL stations, is divided into two sub-arrays. The large sub-array consisting of 57 stations (shown as black triangles in block A in Figure 1) was deployed for more than two years from May 2007 to June 2009 and stations were distributed in the Qiangtang and Songpan-Ganze terranes, as well as in the northernmost Lhasa terrane. A smaller Gansu sub-array of 18 stations was deployed at the southwestern edge of the Ordos block and along the northeastern edge of the Tibetan Plateau from May 2007 to August 2008 (shown as black squares in Block C in Figure 1). From August 2008 to May 2009 18 stations were redeployed in the Qaidam basin and Qilian Mountains (shown as black diamonds in block B in Figure 1). The teleseismic events considered in this study consisted in those with magnitudes between 5.7 and 7.2 mb and ranging in distance from about 86° to 170°. These events are listed in the auxiliary material.¹

4. Methodology

[13] Split shear waves, one fast wave and polarized parallel to the anisotropic fast axis and another slow wave polarized orthogonal to the fast wave, can be used to map the orientation of the upper mantle petrofabrics. Core phases such as PKS, SKS and SKKS are used to infer the lattice preferred orientation in anisotropic upper mantle minerals (mostly olivine) [Silver, 1996; Savage, 1999]. In the absence of partial melt or high water contents, the orientation rotates seismically fast olivine crystallographic *a*-axes into the finite-strain maximum-shear orientation in the case of simple shear [Zhang and Karato, 1995], and into the finite-strain extension orientation for a pure shear [Nicolas *et al.*, 1973].

[14] Shear wave splitting parameters consist of the determination of the orientation of the fast polarization component and the delay time. Most shear wave splitting measurements are based upon particle motion analysis that assumes propagation through a single or two layer anisotropic medium [e.g., Savage, 1999]. In this study we use the grid search method of Silver and Chan [1991] to determine the orientations of fast polarizations and delay time for SKS and SKKS core phases. Assuming one layer of anisotropy with a horizontal axis of symmetry, the shear wave splitting parameters were determined by minimizing the energy in the tangential components by trial and error. We chose sampling windows beginning about 10 s before the SKS and SKKS phase arrival and ending immediately after one period of the phase and analyzed each phase that displaced the elliptical horizontal particle motion indicative of shear wave splitting. After determining parameters that minimized tangential component energy, we checked the fast and slow components visually and that corrected seismograms had linear particle motion. Null measurements, in which no splitting is inferred, are here defined if the estimated delay time is less than 0.4 s for the core phases. Figure 2 shows a complete data set

analysis for station GS16. Figure 3 shows an example seismogram for a station in the high plateau (C010) with a large delay time (2.2 s).

[15] The error analysis utilizes the inverse *F* test, as implemented by Silver and Chan [1991]. The test is performed for each set of possible parameters to determine whether or not the shear wave splitting parameters are within the bounds of a 95% confidence region. We also obtained error estimates using the bootstrap technique of Sandvol and Hearn [1994] with similar results. Only seismograms with variance reduction contours exhibiting clear minima were selected as reliable solutions of splitting parameters. Additionally, a version of the stacking method proposed by Vinnik *et al.* [1989] and Wolfe and Silver [1998] was used for determining the average values. Stacked energies are shown in Figures 2 and 4 for stations GS16 and C010.

[16] In order to evaluate the relationship between the surface and the mantle, we directly compare mantle anisotropy with predicted fast polarization directions from the surface deformation field. We use the method of Haines *et al.* [1998] and Holt *et al.* [2000] to determine a continuous surface deformation field using spline functions to interpolate between observed surface strain rate data inferred from both GPS observations and Quaternary fault slip rates. In order to compare the predicted anisotropy orientations from the instantaneous surface deformation with the observed anisotropy from finite mantle deformation we compare two end-member cases simple-shear and pure-shear deformation. If we assume A-type lattice preferred orientation, the olivine *a*-axis is parallel to the finite-strain maximum shear orientation for simple shear [Zhang and Karato, 1995], and the finite-strain extension orientation for pure shear [Nicolas *et al.*, 1973]. For the simple and pure shear cases the orientation of maximum shear is the same for both instantaneous and finite deformation. Therefore we can use the continuous surface strain rate field to calculate the surface orientation of maximum shear/extension that can then be compared with the observed anisotropy orientations. SKS observations appear to be parallel to the surface-strain instantaneous maximum shear/maximum extension orientation in a simple/pure shear regime. We use the instantaneous surface deformation field from Wang *et al.* [2008] derived from the interpolation of strain rate data inferred from GPS observations and Quaternary fault slip rate data in a Eurasian reference frame to predict mantle anisotropic fabrics. Table 1 summarizes the results for the stations of INDEPTH-IV 2-D and linear arrays.

5. Results

[17] High quality teleseismic core phases, with signal-to-noise ratio greater than 3, were recorded by 65 stations for 87 events. This yielded 927 source-receiver pairs of measurements; 289 were non-null measurements. Individual non-null measurements and surface deformation fields are shown in Figures 5–7 for the 2D array. Average results are shown in Figures 8–11, and summarized in Tables 2–4. Also plotted in these figures is the deformation orientation closest to the fast splitting directions according to the weighted averages of individual measurements. These are either the left-lateral shear, right-lateral shear, or maximum elongation orientation and are computed from GPS and fault slip data [Flesch *et al.*, 2005; Wang *et al.*, 2008]. For stations within the high plateau

¹Auxiliary materials are available in the HTML. doi:10.1029/2011JB008919.

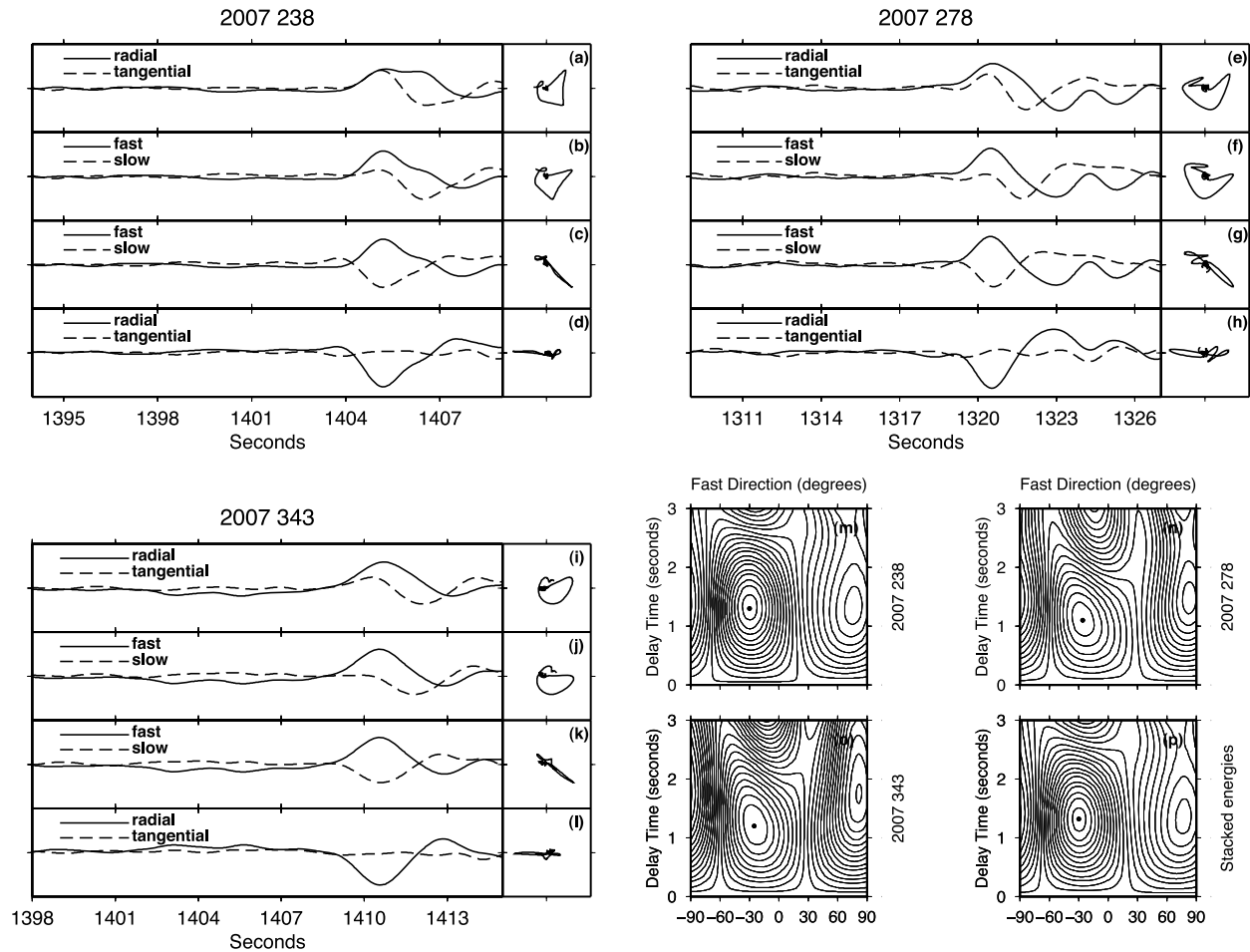


Figure 2. Shear wave splitting analysis for SKS events recorded by station GS16. (a, e, and i) The radial and tangential components, (b, f, and j) the components from Figures 2a, 2e, and 2i rotated to the fast and slow directions, (c, g, and k) the fast and shifted slow components, and (d, h, and l) the radial and tangential components after the energy in the tangential component has been removed. Particle motion is shown to the right of each seismogram. At the top of the seismograms is indicated the year and Julian day of the event. 2007 238 corresponds to an event with back azimuth (BAZ) 110.08° and distance (Δ) 91.99° with fast polarization orientation (φ) $-30^\circ \pm 5^\circ$ and delay time (δt) 1.3 ± 0.2 s. 2007 278 shows the analysis for an event with BAZ = 119.67° , $\Delta = 92.19^\circ$, $\varphi = -26^\circ \pm 10^\circ$, and $\delta t = 1.1 \pm 0.3$ s. 2007 343 illustrates the method for an event with BAZ = 118.60° , $\Delta = 94.84^\circ$, $\varphi = -25^\circ \pm 7^\circ$, and $\delta t = 1.2 \pm 0.2$. (m–p) The corresponding energy plots and the energy plot for the stacked energies. Right labels for energy plots indicate the corresponding events according to the seismogram headers. Black dot shows the best estimate for the shear wave splitting parameters. The first contour around the minimum bounds the 95% confidence region.

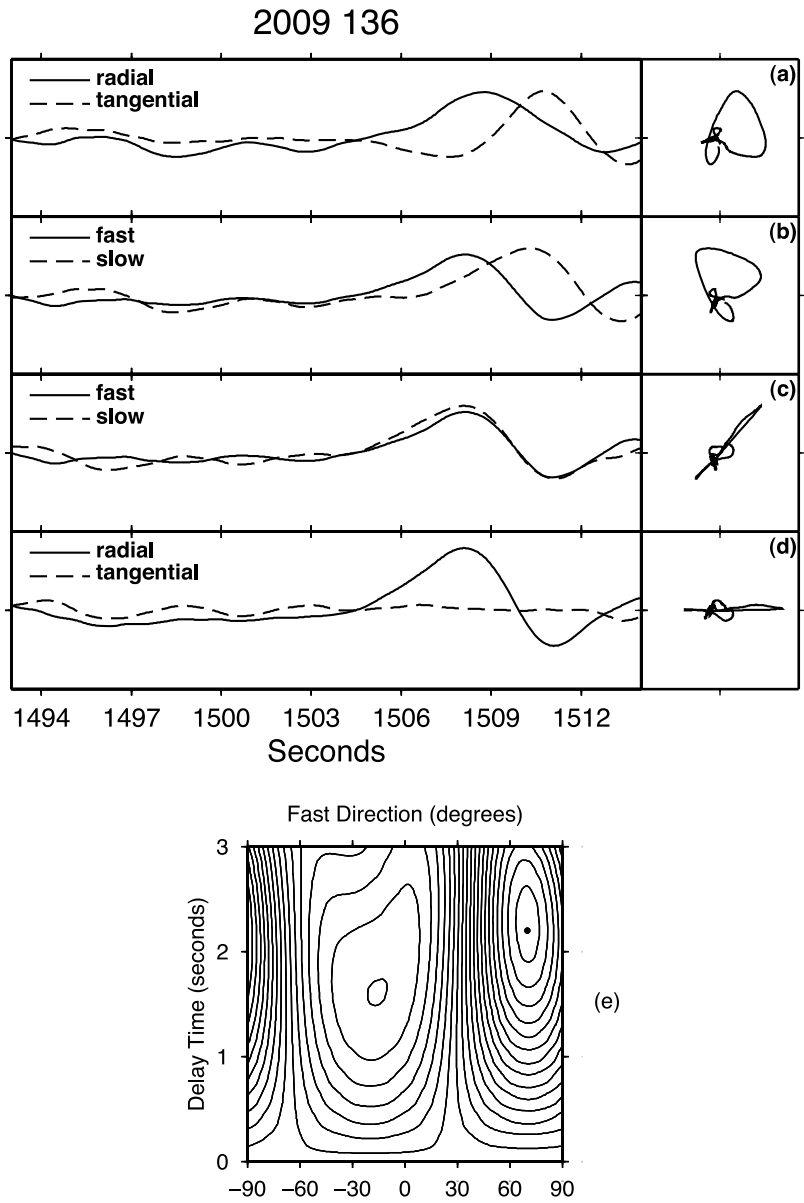


Figure 3. Example seismogram and energy plot for station C010. (a–d) The same meaning as in Figures 2a–2l. (e) The energy plot for this individual measurement. The seismogram corresponds to an event occurred on 2009 136 with $BAZ = 117.32^\circ$, $\Delta = 106.02$, $\varphi = 69^\circ \pm 2^\circ$, and $\delta t = 2.2 \pm 0.1$.

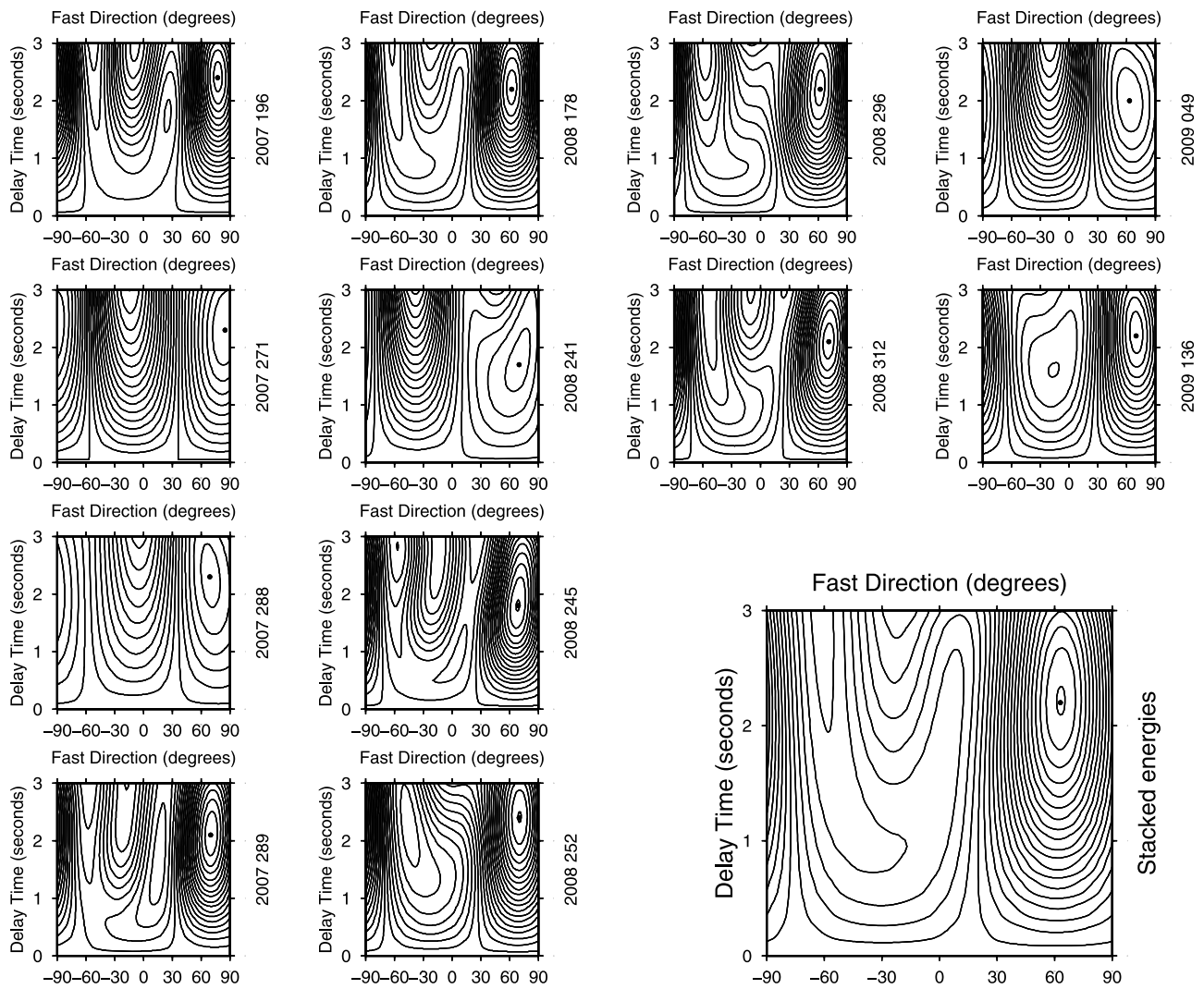


Figure 4. Energy plots from the shear wave splitting analyses and energy plot of the stacked energies for station C010. The right label on each plot indicates the year and Julian day of the event.

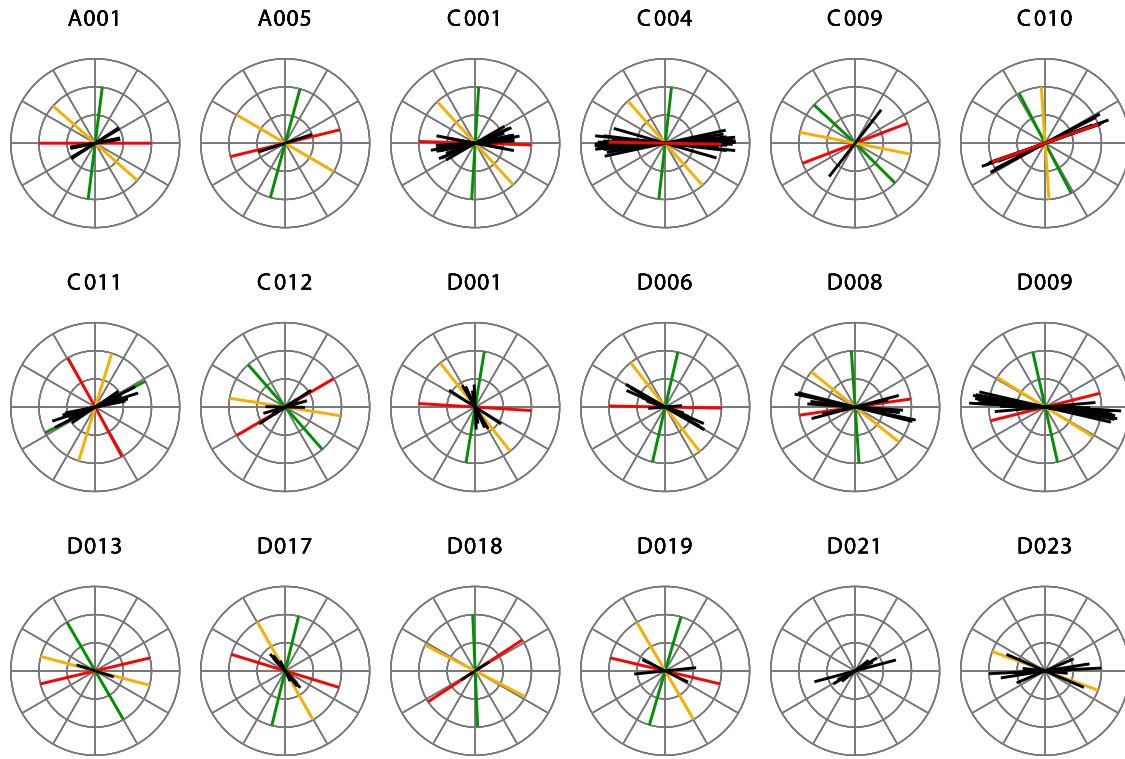


Figure 5. Rose diagrams showing the individual shear wave splitting measurements and surface deformation fields. Each circle represents 1 s of delay time. Black bars stand for the fast polarization orientations. Red lines represent the left-lateral maximum shear orientations, green bars mean right-lateral maximum shear orientation, and yellow lines are the maximum extension orientations.

Table 1. Surface Deformation Fields Inferred From GPS Data^a

Station	Lat (deg)	Lon (deg)	ll-mso (deg)	rl-mso (deg)	Med (deg)
A001	36.43	94.87	0.1	97.1	-41.38
A002	36.79	93.67	0.0	113.3	-33.34
A003	36.91	93.16	6.0	123.4	-25.27
A005	37.02	91.74	13.9	105.3	-30.42
A005	37.02	91.74	13.9	105.3	-30.42
A005	37.02	91.74	13.9	105.3	-30.42
C001	35.81	94.89	-1.8	86.4	132.32
C004	35.57	94.04	-1.0	83.6	131.30
C009	33.86	92.25	21.0	136.9	-11.04
C010	33.26	91.84	19.8	152.6	-3.81
C011	33.79	91.86	24.3	108.9	-23.40
C012	31.99	91.71	30.6	131.2	-9.08
D001	34.18	95.83	-3.7	80.5	128.40
D006	33.76	96.75	-1.2	77.1	127.96
D007	34.78	96.17	4.0	93.4	-41.34
D008	34.92	94.78	8.3	94.1	-38.80
D009	35.12	93.96	14.2	102.7	-31.55
D013	33.01	97.11	30.2	120.1	-14.85
D015	32.85	95.44	-9.7	74.8	122.54
D017	33.73	95.84	-16.9	76.2	119.65
D018	32.89	94.70	33.3	92.5	-27.07
D019	34.27	94.92	-13.2	73.8	120.28
D021	31.87	93.03			
D023	31.54	95.26			-20.02
D023	31.54	95.26			69.98
D024	31.16	96.47	-31.3	48.5	98.61
D025	31.99	96.51	-32.7	18.6	82.95
F001	34.05	96.30	2.8	81.5	132.17
F002	33.83	97.10	-4.4	73.3	124.46
F004	32.33	95.97	-61.1	-41.5	38.71
F005	32.30	96.43	-13.7	15.0	90.68
F006	33.10	95.11	-12.6	72.5	119.96
F012	31.51	96.32	-35.0	23.9	84.45
F013	31.24	95.91	-14.0	43.4	104.71
F014	31.56	94.65	24.4	92.8	-31.41
F015	31.87	93.78	12.2	85.8	-40.98
F016	31.69	92.42	176.7	105.8	-38.77
F017	32.39	91.71	30.9	98.4	-25.36
GS01	34.27	104.24	-52.6	26.2	76.82
GS02	33.78	102.97	-25.4	63.4	109.03
GS03	34.43	102.29	-26.9	69.9	111.48
GS04	35.05	104.57	163.3	124.1	36.30
GS05	34.65	103.54	-27.7	34.1	93.20
GS07	34.45	105.04	159.7	121.4	-39.46
GS08	33.48	105.00	0.8	81.1	130.96
GS09	32.87	106.46	-61.8	27.3	72.75
GS10	33.54	106.91	24.7	143.7	-5.82
GS11	33.91	105.97			
GS12	34.85	105.75	-16.8	76.7	119.95
GS13	35.64	105.45	-3.6	80.4	128.38
GS14	35.70	104.53	-2.9	73.8	125.47
GS15	35.38	107.34			-12.95
GS15	35.38	107.34			77.05
GS16	36.05	106.06	-49.2	61.3	96.01
GS18	32.87	104.78	-84.7	33.4	64.36
H001	36.21	96.39	0.0	90.3	-44.82
H002	36.27	96.96	1.3	82.5	131.90
H003	35.90	97.98	-5.2	69.3	122.10
H004	35.94	97.49	-6.1	70.7	122.30
H005	35.66	98.41	-8.9	79.9	125.51
H006	36.28	98.12	6.7	97.6	-37.81
H008	36.77	98.96	8.3	123.7	-24.04
H009	37.61	99.39	1.5	105.2	-36.63
H010	37.68	98.63	2.8	109.9	-33.64
H013	36.97	97.65	38.5	137.9	-1.84
H014	37.35	96.75	5.8	99.3	-37.44
H017	38.03	94.55	-41.2	48.7	93.76
H018	37.68	93.66			
H019	38.26	92.14	18.5	148.8	-6.36
H020	38.80	94.35	16.1	117.7	-23.09
H021	39.58	94.27	22.7	103.1	-27.11

Table 1. (continued)

Station	Lat (deg)	Lon (deg)	ll-mso (deg)	rl-mso (deg)	Med (deg)
H022	39.76	93.49	16.8	106.0	-28.62
H023	39.51	94.90	5.8	101.3	-36.45
JSO1	35.43	93.45	5.6	91.9	-41.25
JSO2	35.17	92.99	-2.3	81.2	129.47
JSO3	34.38	92.77	-18.0	60.4	111.20
JSO25	34.64	92.80	-15.8	59.0	111.59
KF101	35.64	95.09	-1.7	84.6	131.47
KF106	35.69	95.09	-1.8	84.4	131.32
KF111	35.76	94.97	-1.7	85.5	131.89
KF116	35.80	94.90	-1.8	86.3	132.25
KF141	36.03	94.81	-3.5	76.8	126.62
KF146	36.07	94.79	-4.4	75.5	125.52
KF151	36.13	94.76	-6.5	74.1	123.82
KF66A	35.35	94.95	1.3	91.8	-43.45
KF71A	35.39	94.94	0.8	92.2	-43.50
KF76A	35.44	94.94	0.2	90.5	-44.62
KF81A	35.48	94.98	-0.4	88.7	134.11
KF91A	35.55	95.08	-1.4	86.0	132.29
KF96A	35.60	95.10	-1.6	85.0	131.71
KF86N	35.51	95.05	-1.0	87.3	133.12

^aAngles are with respect to the east. Blank spaces mean no deformation. ll-mso stands for left-lateral maximum shear orientation, rl-mso for right-lateral maximum shear orientation, and med for maximum extension orientation.

we found polarization orientations independent of back azimuth (see for example Figure 12 for station C010), suggesting that a single layer with a horizontal symmetry axis is sufficient to explain the data. These measurements are, in general, consistent with those of previous studies [McNamara *et al.*, 1994; Sol *et al.*, 2007; Wang *et al.*, 2008]. Splitting parameters for stations near Banggong-Nujiang Suture (BNS) (C011, C012, D021, D023, D024, F012, F013, F014, F015, and F017 in Figure 8) are consistent with the results of Sol *et al.* [2007]. The fast polarization orientations tend to follow the surface trace of the BNS and the sinistral shear zones with delay times of about 1.0 s. Shear wave splitting parameters of stations near the Kunlun Fault and within the Songpang-Ganzi and Qiangtang terrane (stations C004, C009, C010, C011, D008, D009, and F017) (Figure 8) are similar to those reported by McNamara *et al.* [1994] and the fast polarization orientations are oriented from NE-SW in the south to E-W in the north. Three stations on the Qiangtang terrane (C009, C010, and C011) show large delay times up to 2.2 s. Shear wave splitting parameters for stations on the Songpang-Ganzi terrane and near the Kunlun fault (C004, D008, and D009) exhibit an E-W trend of fast polarization orientations with delay times in the range 1.6–2.2 s. The station coverage in this study spans some sparsely characterized regions in northeastern Tibet. Stations D001, D006, D013, D017, D019, F001, and F002 (Figure 8) present fast polarizations in the orientation of the local strike-slip faulting with delay times between 0.6–1.0 s.

[18] Stations in the Gansu sub-array (Figure 9) are located in a region of mainly strike-slip faulting and most of the seismic anisotropy measurements for these stations near major faults exhibit fast polarization orientations sub-parallel to E-W trending strike-slip faults. However, for a few stations within fault blocks, the fast polarization orientations are oblique to the trends of local faults.

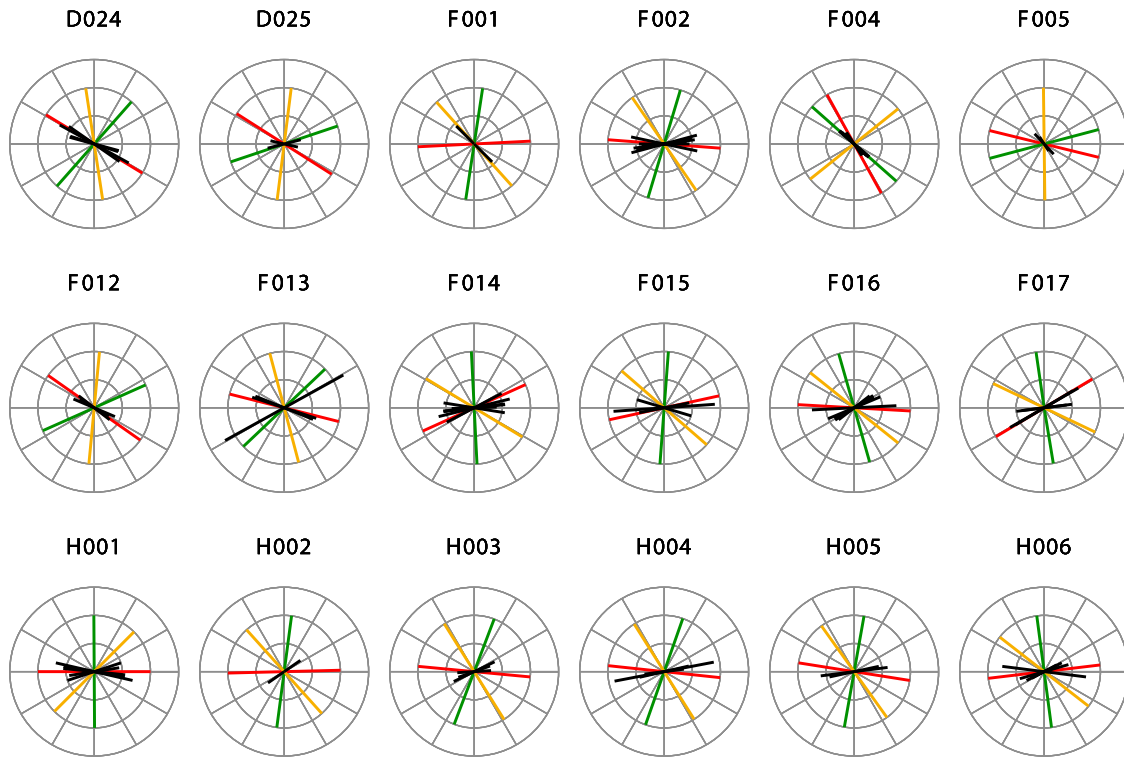


Figure 6. Rose diagrams showing the individual shear wave splitting measurements and surface deformation fields. Color code is the same as Figure 5.

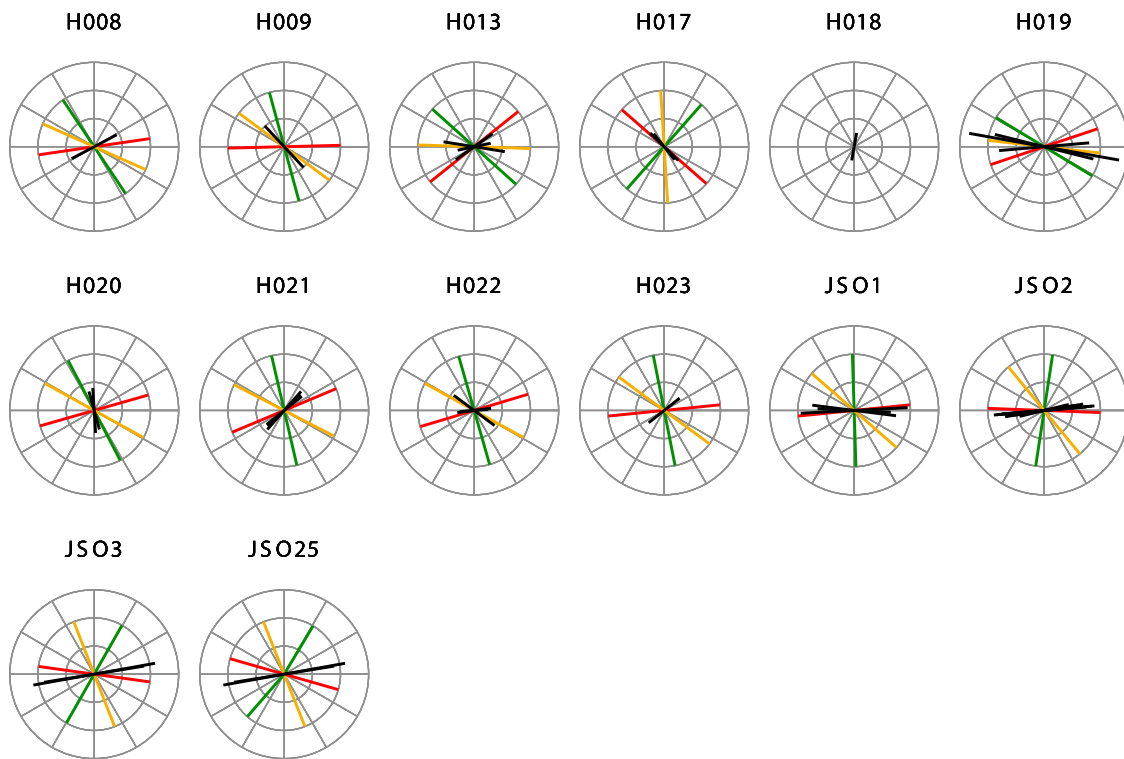


Figure 7. Rose diagrams showing the individual shear wave splitting measurements and surface deformation fields. Color code is the same as Figure 5.

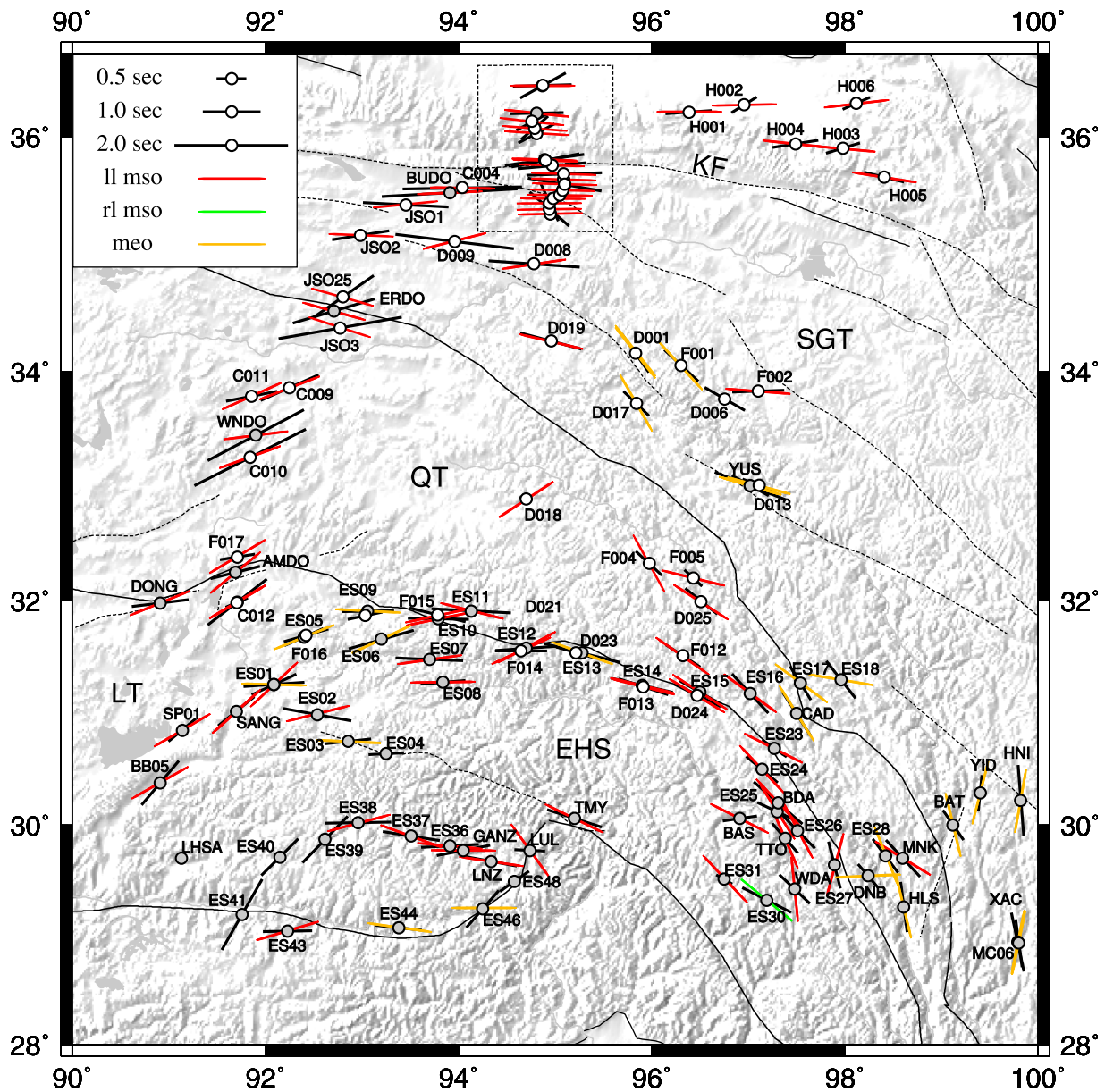


Figure 8. Map displaying shear wave splitting parameters for the INDEPTH-IV 2-D array. Black bars represent the averaged orientations of fast orientations of polarization and the lengths are proportional to the corresponding delay times according to the figure caption. Red, green and yellow bars are the left-lateral maximum shear orientation (ll mso), right-lateral maximum shear orientation (rl mso), and maximum elongation orientation (meo), calculated from GPS and fault slip data, respectively. White circles are the results reported in this article. Gray circles correspond to results reported by previous studies. QT stands for Qiangtang Terrane, LS for Lhasa Terrane, SGT for Songpan Ganzi Terrane, EHS for Eastern Himalayan Syntaxis, and KF for Kunlun Fault.

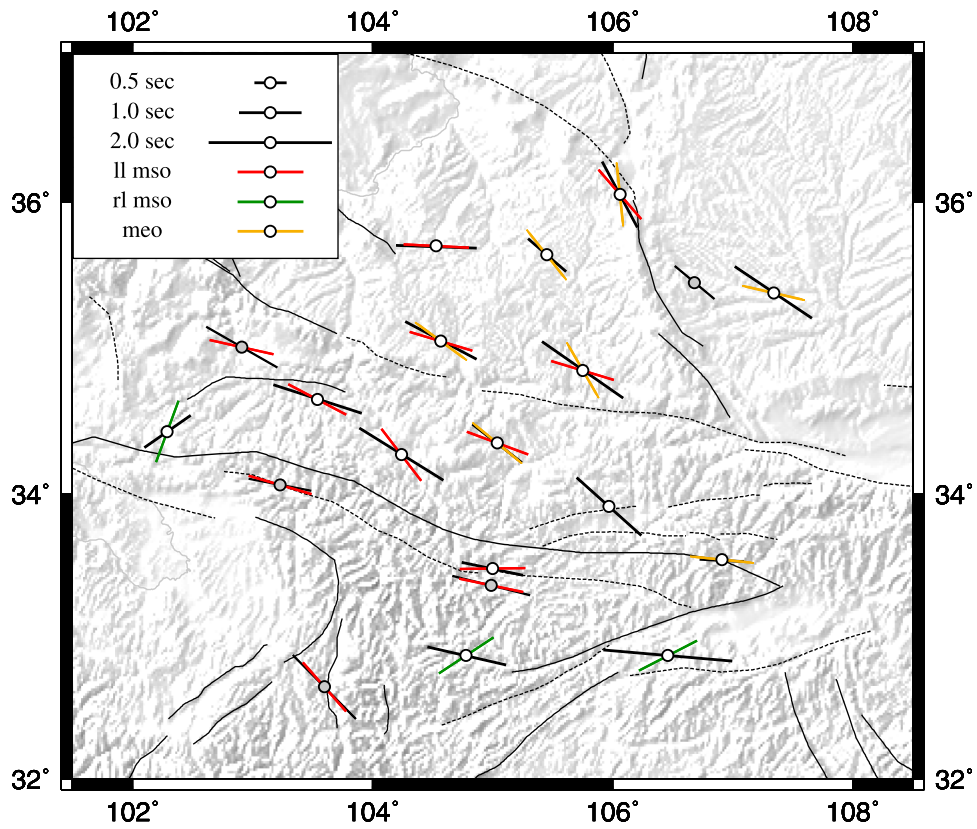


Figure 9. Map displaying shear wave splitting parameters of the 18 station northeastern Tibet array. Color code is the same as in Figure 8.

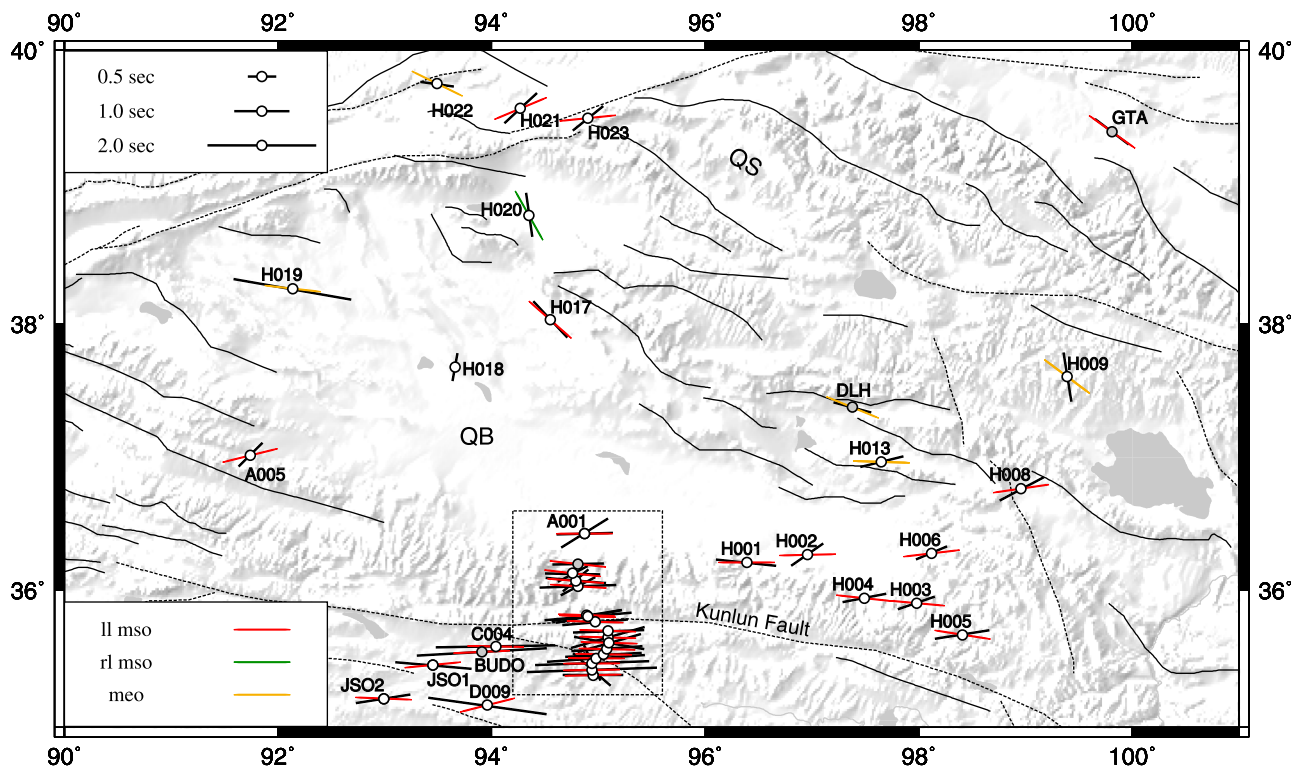


Figure 10. Map displaying shear wave splitting parameters of the Qaidam Basin (QB) and Qilian Shan (QS) array. Symbols are the same as in Figure 8.

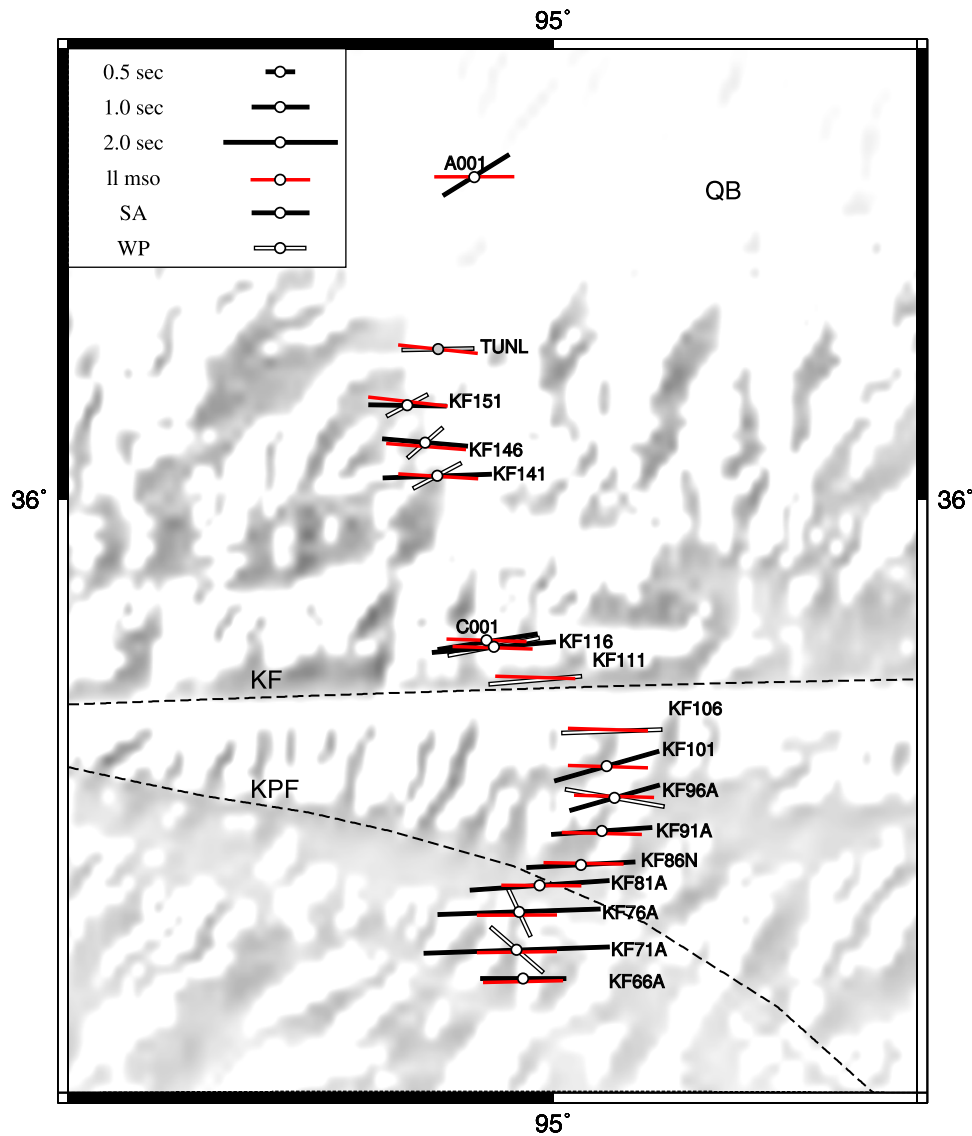


Figure 11. Map displaying shear wave splitting parameters of the INDEPTH-IV 1D linear array in the vicinity of the Kunlun fault. Black bars stand for the averaged fast polarization orientations from events in South America. Open bars represent the averaged fast polarization directions computed from event from Western Pacific. Red bars are the left-lateral maximum shear orientation. KF stands for Kunlun Fault, KPF for Kunlun Pass Fault, QB for Qaidam Basin.

Table 2. Weighted Averages for the 2-D Array^a

Station	Lat (deg)	Lon (deg)	Fast (deg) SC	Delay (s) SC	Fast (deg) VW	Delay (s) VW
A001	36.4327	94.8732	58.0 ± 5.0	1.1 ± 0.1	61.0 ± 5.0	0.9 ± 0.1
A005	37.0236	91.7443	45.0 ± 5.0	0.6 ± 0.1	85.0 ± 9.0	0.3 ± 0.1
C001	35.8080	94.8920	81.0 ± 2.0	1.3 ± 0.3	82.0 ± 5.0	1.4 ± 0.1
C004	35.5709	94.0377	89.0 ± 1.0	2.2 ± 0.1	89.0 ± 1.0	2.1 ± 0.1
C009	33.8612	92.2509	64.0 ± 1.0	1.1 ± 0.1	66.0 ± 1.0	1.1 ± 0.1
C010	33.2580	91.8440	69.0 ± 2.0	2.2 ± 0.1	63.0 ± 2.0	2.2 ± 0.1
C011	33.7864	91.8598	73.0 ± 2.0	1.2 ± 0.1	79.0 ± 1.0	0.9 ± 0.1
C012	31.9859	91.7069	70.0 ± 6.0	0.6 ± 0.1	67.0 ± 4.0	0.4 ± 0.1
D001	34.1576	95.8316	-28.0 ± 5.0	0.8 ± 0.1	-35.0 ± 2.0	0.8 ± 0.1
D006	33.7630	96.7545	-62.0 ± 1.0	1.0 ± 0.1	-60.0 ± 1.0	0.8 ± 0.1
D008	34.9240	94.7810	-85.0 ± 4.0	1.6 ± 0.2	-86.0 ± 2.0	1.6 ± 0.1
D009	35.1154	93.9611	-82.0 ± 1.0	2.2 ± 0.1	-83.0 ± 1.0	2.1 ± 0.1
D013	33.0123	97.1132	-72.0 ± 16.0	0.7 ± 0.2	-69.0 ± 1.0	0.6 ± 0.1
D017	33.7249	95.8419	-41.0 ± 5.0	0.6 ± 0.1	-46.0 ± 1.0	0.6 ± 0.1
D018	32.8941	94.7009	57.0 ± 15.0	0.6 ± 0.2	74.0 ± 13.0	0.2 ± 0.2
D019	34.2641	94.9584	88.0 ± 6.0	1.0 ± 0.2	-75.0 ± 1.0	1.1 ± 0.1
D021	31.8697	93.0330	68.0 ± 6.0	0.8 ± 0.1	78.0 ± 7.0	0.6 ± 0.1
D023	31.5421	95.2145	-82.0 ± 2.0	0.9 ± 0.1	-74.0 ± 2.0	0.7 ± 0.1
D024	31.1610	96.4715	-61.0 ± 4.0	1.0 ± 0.2	-64.0 ± 4.0	0.9 ± 0.1
D025	31.9944	96.5116	84.0 ± 12.0	0.6 ± 0.2	-51.0 ± 2.0	0.7 ± 0.1
F001	34.0535	96.3041	-45.0 ± 7.0	0.9 ± 0.2	-47.0 ± 3.0	0.8 ± 0.1
F002	33.8331	97.1024	87.0 ± 4.0	1.0 ± 0.1	88.0 ± 5.0	0.9 ± 0.1
F004	32.3314	95.9731	-46.0 ± 5.0	0.6 ± 0.1	-47.0 ± 1.0	0.6 ± 0.1
F005	32.2003	96.4311	-39.0 ± 15.0	0.4 ± 0.1	47.0 ± 2.0	0.4 ± 0.1
F012	31.5140	96.3244	-59.0 ± 8.0	0.7 ± 0.1	-57.0 ± 4.0	0.7 ± 0.1
F013	31.2393	95.9134	-77.0 ± 8.0	1.1 ± 0.3	-72.0 ± 1.0	0.9 ± 0.1
F014	31.5572	94.6493	82.0 ± 5.0	1.0 ± 0.2	90.0 ± 3.0	0.9 ± 0.1
F015	31.8746	93.7837	90.0 ± 7.0	1.1 ± 0.3	-76.0 ± 3.0	1.0 ± 0.1
F016	31.6949	92.4233	73.0 ± 5.0	1.0 ± 0.1	74.0 ± 6.0	0.8 ± 0.1
F017	32.3861	91.7105	65.0 ± 5.0	1.1 ± 0.1	81.0 ± 4.0	0.6 ± 0.1
GS01	34.2720	104.2420	-58.0 ± 3.0	1.6 ± 0.2	-57.0 ± 3.0	1.6 ± 0.2
GS03	34.4300	102.2940	55.0 ± 3.0	0.9 ± 0.1	60.0 ± 6.0	0.7 ± 0.1
GS04	35.0550	104.5710	-62.0 ± 2.0	1.3 ± 0.2	-65.0 ± 3.0	1.0 ± 0.2
GS05	34.6520	103.5430	-72.0 ± 3.0	1.5 ± 0.1	-68.0 ± 2.0	1.5 ± 0.2
GS07	34.3483	105.0387	-52.0 ± 6.0	1.0 ± 0.2	-58.0 ± 3.0	1.0 ± 0.2
GS08	33.4760	104.9980	-78.0 ± 5.0	1.0 ± 0.2	-76.0 ± 2.0	0.9 ± 0.1
GS09	32.8695	106.4587	-85.0 ± 7.0	2.1 ± 0.6	-85.0 ± 12.0	2.1 ± 0.8
GS10	33.5360	106.9060	-87.0 ± 17.0	0.7 ± 0.3	-69.0 ± 3.0	0.6 ± 0.2
GS11	33.9110	105.9690	-48.0 ± 13.0	1.4 ± 0.5	-64.0 ± 2.0	0.8 ± 0.2
GS12	34.8530	105.7500	-55.0 ± 6.0	1.6 ± 0.4	-64.0 ± 4.0	0.7 ± 0.2
GS13	35.6360	105.4530	-49.0 ± 4.0	0.8 ± 0.1	-52.0 ± 2.0	0.8 ± 0.1
GS14	35.6950	104.5320	-88.0 ± 5.0	1.3 ± 0.2	-66.0 ± 3.0	1.0 ± 0.2
GS15	35.3830	107.3360	-56.0 ± 3.0	1.5 ± 0.3	-55.0 ± 5.0	1.1 ± 0.3
GS16	36.0480	106.0590	-28.0 ± 4.0	1.2 ± 0.1	-32.0 ± 3.0	1.2 ± 0.1
GS18	32.8660	104.7850	-77.0 ± 4.0	1.3 ± 0.2	-69.0 ± 2.0	1.2 ± 0.1
H001	36.2090	96.3850	-84.0 ± 4.0	1.1 ± 0.2	86.0 ± 2.0	0.8 ± 0.1
H002	36.2690	96.9560	55.0 ± 6.0	0.7 ± 0.2	58.0 ± 6.0	0.5 ± 0.1
H003	35.9040	97.9780	71.0 ± 6.0	0.7 ± 0.1	73.0 ± 3.0	0.6 ± 0.1
H004	35.9410	97.4910	79.0 ± 3.0	0.8 ± 0.1	81.0 ± 2.0	0.8 ± 0.1
H005	35.6610	98.4080	81.0 ± 6.0	1.0 ± 0.2	-76.0 ± 10.0	0.7 ± 0.2
H006	36.2820	98.1200	67.0 ± 4.0	0.6 ± 0.1	66.0 ± 2.0	0.5 ± 0.1
H008	36.7660	98.9630	62.0 ± 10.0	0.9 ± 0.2	63.0 ± 15.0	0.5 ± 0.2
H009	37.6060	99.3930	-9.0 ± 16.0	0.9 ± 0.5	-2.0 ± 17.0	0.3 ± 0.1
H013	36.9730	97.6540	76.0 ± 9.0	0.8 ± 0.2	63.0 ± 3.0	0.3 ± 0.1
H017	38.0340	94.5520	-43.0 ± 17.0	0.6 ± 0.2	-26.0 ± 12.0	0.3 ± 0.1
H018	37.6800	93.6560	10.0 ± 9.0	0.5 ± 0.3	-6.0 ± 15.0	0.2 ± 0.1
H019	38.2560	92.1370	-80.0 ± 1.0	2.2 ± 0.3	18.0 ± 8.0	0.2 ± 0.2
H020	38.8050	94.3530	-8.0 ± 11.0	0.8 ± 0.2	-5.0 ± 8.0	0.6 ± 0.1
H021	39.5810	94.2720	47.0 ± 5.0	0.8 ± 0.2	46.0 ± 3.0	0.8 ± 0.1
H022	39.7560	93.4890	-82.0 ± 8.0	0.6 ± 0.1	75.0 ± 14.0	0.2 ± 0.1
H023	39.5060	94.9040	51.0 ± 13.0	0.7 ± 0.2	75.0 ± 16.0	0.3 ± 0.1
JSO1	35.4250	93.4550	-85.0 ± 3.0	1.4 ± 0.2	-87.0 ± 4.0	1.4 ± 0.2
JSO2	35.1690	92.9850	75.0 ± 12.0	1.1 ± 0.1	81.0 ± 4.0	1.0 ± 0.1
JSO3	34.3750	92.7750	80.0 ± 2.0	2.0 ± 0.1	80.0 ± 2.0	2.2 ± 0.1
JSO25	34.6429	92.8038	58.0 ± 3.0	1.0 ± 0.1	55.0 ± 4.0	1.3 ± 0.1

^aAngles are with respect to the north. Fourth and fifth columns correspond to the average values from the individual measurements. Sixth and seventh columns are the stacked average values from the *Vinnik et al.* [1989] and *Wolfe and Silver* [1998] approaches.

Table 3. Weighted and Stacked Averages for the 1-D Array for Events From the Western Pacific^a

Station	Lat (deg)	Lon (deg)	Fast (deg) SC	Delay (s) SC	Fast (deg) VW	Delay (s) VW
KF106	35.6878	95.0968	88.0 ± 3.0	1.3 ± 0.1	89.0 ± 4.0	1.3 ± 0.2
KF111	35.7558	94.9697	85.0 ± 3.0	1.2 ± 0.1	83.0 ± 3.0	1.2 ± 0.1
KF116	35.8010	94.9022	79.0 ± 3.0	1.2 ± 0.1	77.0 ± 4.0	1.3 ± 0.1
KF141	36.0305	94.8088	62.0 ± 7.0	0.7 ± 0.1	63.0 ± 10.0	0.6 ± 0.1
KF146	36.0750	94.7887	49.0 ± 6.0	0.6 ± 0.1	47.0 ± 5.0	0.8 ± 0.1
KF151	36.1250	94.7594	62.0 ± 6.0	0.6 ± 0.1	59.0 ± 7.0	0.6 ± 0.1
KF71A	35.3929	94.9397	−49.0 ± 10.0	0.9 ± 0.2	−53.0 ± 10.0	1.0 ± 0.3
KF76A	35.4444	94.9435	−25.0 ± 22.0	0.7 ± 0.3		
KF96A	35.5980	95.1013	−80.0 ± 4.0	1.3 ± 0.3		

^aColumn description is the same as in Table 2. Blank spaces indicate measurements constrained with 1 measurement.

[19] Stations H002, H003, H004, H005, and H006 (Figure 10) deployed on the southeastern Qaidam basin just to the north of the Kunlun fault show small delay times with fast polarization orientations oblique to the E-W striking Kunlun fault. Station H001 (Figures 8 and 10) located closer to the Kunlun fault has a fast polarization orientation that is parallel to the fault. Stations H021 and H023, located near Altyn Tagh fault, show a fast polarization orientation that is sub-parallel to the fault. Fast polarization orientations at stations A005, H018, and H0020 (Figure 10), located in the western part of the Qaidam basin, do not correlate with the local geologic features. Fast polarization orientations at stations H008, and H009, located in the southern Qiling Shan, show little correlation with local geology. Moreover, many stations show some azimuthal dependence of the shear wave splitting parameters. In particular, station A005 recorded 50 events with good quality from which only 7 reliable splitting parameters could be resolved, and the rest yielded null measurements.

[20] Across the Kunlun fault, seismic anisotropy measurements at stations C001, KF101, KF106, KF111, KF116, KF81A, KF86N, KF91A and KF96A (Figure 11) show fast polarization orientations trending approximately E-W, parallel to the strike of the Kunlun fault. For stations located just north of the Kunlun fault (station KF141, KF146 and KF151 in Figure 11), fast polarization orientations are also oriented E-W for SKS waves originating in South America (SA),

however, small delay time (~ 0.6 s) and a NE-SW oriented fast polarization orientation were found for events from the West Pacific (WP). We found mostly E-W fast polarization orientations for stations located south of the Kunlun fault, however, two stations, KF71A and KF76A (Figure 11), near Xianshuihe-Xiaojiang fault zone (XXF) show NW-SE fast polarization orientations with small delay time (0.8 s) from an event from the South Pacific.

6. Discussion

[21] Within the eastern Tibetan plateau, the fast polarization orientations reveal a clockwise rotation pattern from NE-SW, to E-W, to NW-SE, and then to N-S. The N-S oriented fast polarization orientation abruptly changes to E-W below latitude $\sim 27^\circ\text{N}$ above the northern edge of the Burma slab [Lev *et al.*, 2006; Sol *et al.*, 2007; Li *et al.*, 2008; Wang *et al.*, 2008]. The shear wave splitting observations from INDEPTH-IV show a generally good correlation with the surficial geological features for stations located south of the Kunlun fault. In order to determine the misfit between the observed fast polarization orientations and the surface deformation fields we use an inverse F test applied to the directional data [Trauth, 2007]. The detail of the F-statistic for assessing the consistency of two sets of orientations is giving in Appendix A. For the northeastern Tibet we found that the fast polarization orientations match the left-lateral

Table 4. Weighted and Stacked Averages for the 1-D Array for Events From South America^a

Station	Lat (deg)	Lon (deg)	Fast (deg) SC	Delay (s) SC	Fast (deg) VW	Delay (s) VW
KF101	35.6409	95.0882	74.0 ± 2.0	1.4 ± 0.1	74.0 ± 2.0	1.4 ± 0.1
KF106	35.6878	95.0968	70.0 ± 4.0	1.6 ± 0.2	69.0 ± 2.0	1.6 ± 0.1
KF111	35.7558	94.9697	73.0 ± 5.0	1.5 ± 0.2		
KF116	35.8010	94.9022	85.0 ± 4.0	1.6 ± 0.2	84.0 ± 3.0	1.6 ± 0.2
KF141	36.0305	94.8088	88.0 ± 6.0	1.4 ± 0.3	89.0 ± 8.0	1.4 ± 0.2
KF146	36.0750	94.7887	−85.0 ± 10.0	1.1 ± 0.3		
KF151	36.1250	94.7594	−89.0 ± 6.0	1.0 ± 0.1	89.0 ± 4.0	0.9 ± 0.1
KF66A	35.3540	94.9505	90.0 ± 7.0	2.2 ± 0.6		
KF71A	35.3929	94.9397	88.0 ± 4.0	2.4 ± 0.3	−89.0 ± 5.0	2.4 ± 0.3
KF76A	35.4444	94.9435	88.0 ± 3.0	2.1 ± 0.2	88.0 ± 3.0	2.1 ± 0.2
KF81A	35.4801	94.9874	86.0 ± 4.0	1.8 ± 0.2	86.0 ± 3.0	1.9 ± 0.2
KF86N	35.5076	95.0459	87.0 ± 5.0	1.4 ± 0.2	89.0 ± 6.0	1.5 ± 0.2
KF91A	35.5535	95.0802	86.0 ± 5.0	1.3 ± 0.2	90.0 ± 4.0	1.2 ± 0.1
KF96A	35.5980	95.1013	74.0 ± 8.0	1.2 ± 0.2	−84.0 ± 8.0	1.2 ± 0.4

^aColumn description is the same as in Table 2. Blank spaces indicate measurements constrained with 1 measurement.

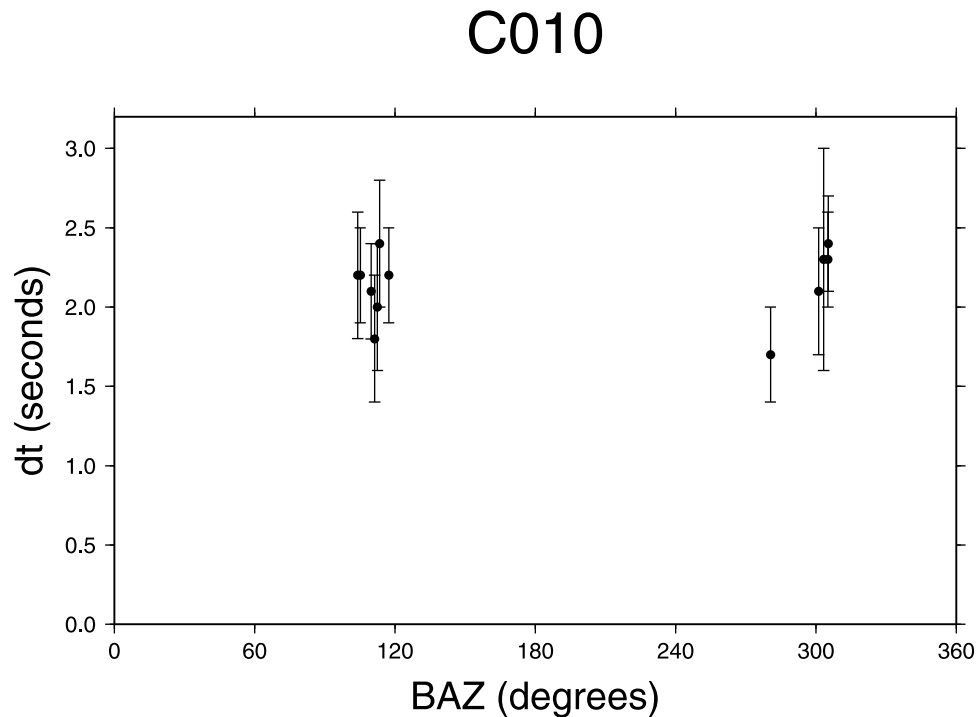


Figure 12. Delay time (dt) versus back azimuth (BAZ) for station C010 showing an apparent independence of dt from BAZ. Vertical bars represent the uncertainty of the measurement.

maximum shear orientation, but do not match the right-lateral maximum shear orientation nor the elongation orientation (Figure 13). To the north of the Kunlun fault, in Qaidam basin, splitting parameters show no apparent correlation with the surface features, maximum-shear and maximum extension or GPS velocity fields. Small delay times, as well as a large number of null measurements and some indication of azimuthal dependence of the shear wave splitting parameters, indicate a complex anisotropic regime that could be caused by multiple layers of anisotropy. Southernmost INDEPTH-IV stations D023, D024, F012, F013, F014, F015 (Figure 8) are located on a road that approximately follows the BNS and E-W to NW-SE trending strike-slip faults, which cut across the Eastern Himalayan Syntaxis. The fast polarizations of split core phases approximately follow a clockwise rotation of the surface velocity observed from GPS data (Figure 8). These fast polarization orientations also present a good correlation with the left-lateral maximum shear orientation (Figure 8) calculated from gravitational potential energy differences and boundary conditions within the lithosphere and a first order contribution of deviatoric stresses associated with stress boundary conditions [Flesch *et al.*, 2001; Wang *et al.*, 2008], suggesting strong mechanical coupling between the crust and lithospheric mantle.

[22] Since shear wave splitting is the integrated effect along the entire raypath, anisotropy recorded by core phases may be anywhere between the core-mantle boundary and the receiver. The contribution of the crust to the measured anisotropy is very small (~ 0.3 s) and is mainly located in the uppermost 20 km of the crust [McNamara *et al.*, 1994; Weeraratne *et al.*, 2009]. Although some petrophysical studies have suggested that the crustal contribution to

anisotropy could be of the order of 1 s/10 km [Barruol and Mainprice, 1993], nearly all measurements of crustal anisotropy using surface wave and local earthquakes show that the value is much less than this [e.g., Savage, 1999]. Crustal thickness in the Eastern Himalayan Syntaxis varies from 60 to 75 km [Sun *et al.*, 2008]. We can estimate the thickness of the anisotropic layer and compare it to the lithospheric thickness (Table 5). It has been suggested that the lithosphere beneath the BNS could be as thick as 160–170 km [Kumar *et al.*, 2006]. Since the anisotropic layer has a thickness of about 120 km (Table 5), this implies that the observed anisotropy resides mainly in the continental lithosphere with only a very minor component in the asthenosphere.

[23] The curved pattern of fast polarization directions in the Eastern Himalayan Syntaxis region is similar to the fast anisotropic orientation observed from surface waves at depth of 150 km [Yao *et al.*, 2010]. If the deeper seismic anisotropy is related to the flow of the asthenosphere, then poloidal and toroidal flows associated with a roll-back of Burma slab could be the most likely candidate of some of the observed anisotropy. As the Burma slab sinks into the mantle, the trench retreats westward, pulling the trailing plate into the mantle poloidal flow develops in the back arc of the Burma subduction zone (Panxi rift). Toroidal flows develop at the northern open edge of the slab since the subslab mantle material is forced around the slab as a consequence of rolling back. Toroidal flow, inferred from seismic anisotropy, has recently become recognized in many subduction zones, for example, in western Italy [Civello and Margheriti, 2004], Kamchatka [Peyton *et al.*, 2001], and in western Mexico [León Soto *et al.*, 2009], as well as in continental collision

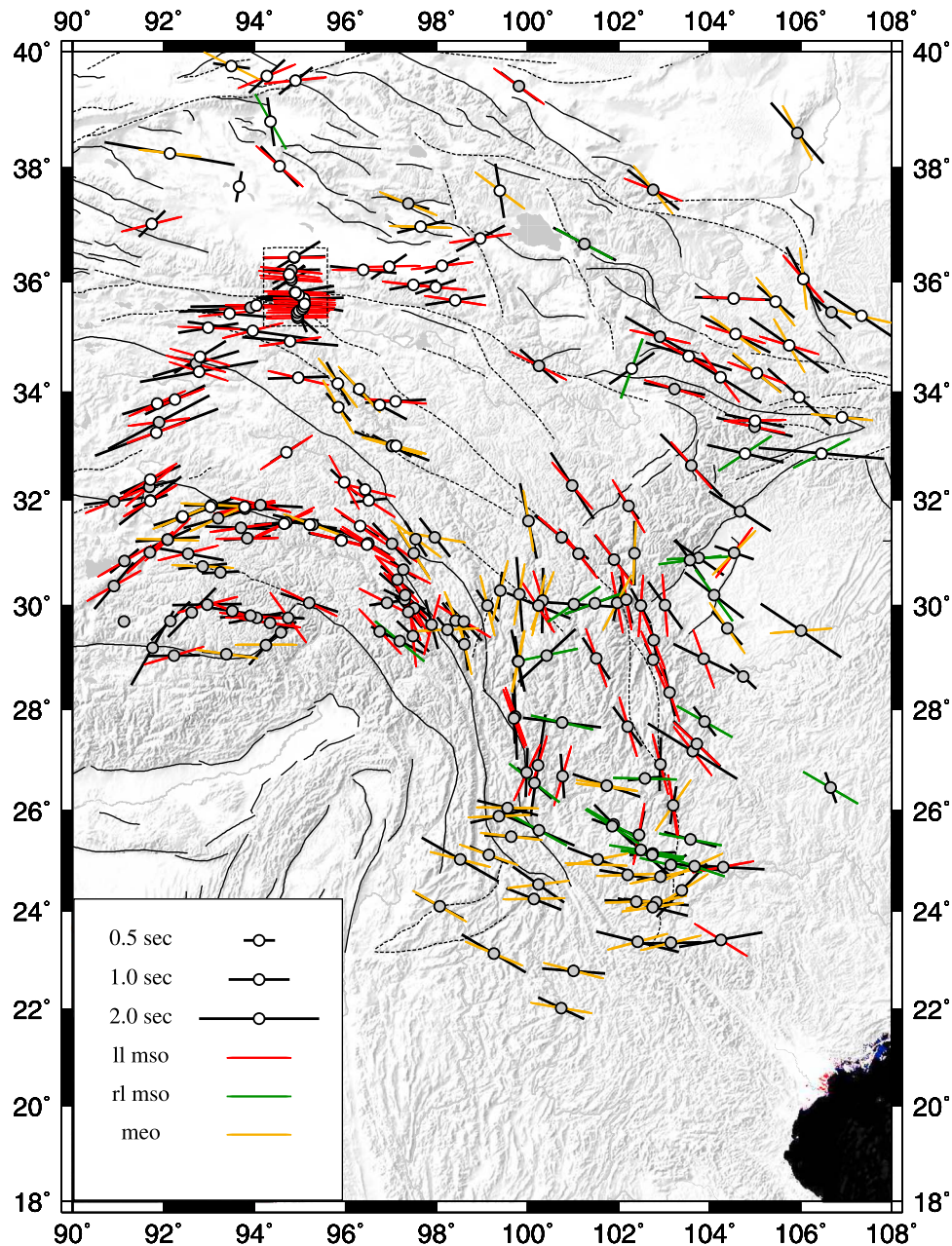


Figure 13. Comparison between observed splitting orientation (black bars) and anisotropic orientation from the surface deformation fields. Note the strong correlation of left-lateral maximum shear orientation and observed fast splitting orientation in much of the eastern Tibet. The Yunnan province, located in the Burma back arc region, is under E-W extension where the fast splitting orientations are sub-parallel to the maximum elongation orientations.

zones such as beneath the western Alps [Barruol *et al.*, 2011]. The rotation pattern of seismic anisotropy and related finite-strain suggests that the kinematic and dynamic of the deformation in the Eastern Himalayan Syntaxis could be related to the foundering Burma slab, which probably causes the bending and shearing of the lithosphere beneath the Eastern Himalayan Syntaxis. A full understanding of the dynamics of the Eastern Himalayan Syntaxis requires investigation of how the foundering of the Burma slab affects the deformation of the Eastern Himalayan Syntaxis.

Table 5. Estimation of the Thickness of the Anisotropic Layer From the Delay Times^a

	Δt (s)	Anisotropic Layer Thickness	Crustal Thickness	Lithospheric Thickness
EHS	1.1	124 km	60–75 km	160–170 km
Gansu	1.1	124 km	50 km	120 km
GS09	2.1	236 km	50 km	120 km
QT and SGT	2.2	248 km	70 km	160 km

^aA 4% anisotropy and a shear velocity of 4.5 km/s are assumed. EHS = Eastern Himalayan Syntaxis, QT = Qiangtang Terrane, SGT = Songpan-Gazi Terrane.

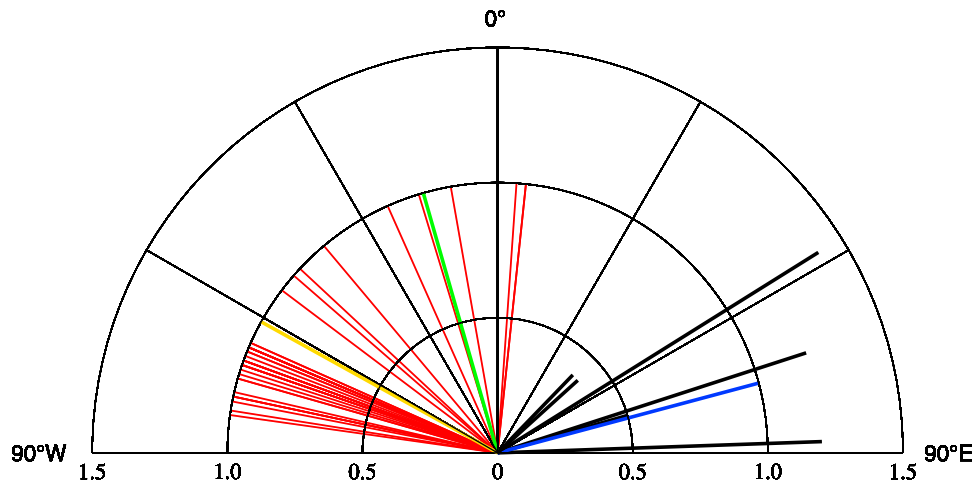


Figure 14. Rose diagram showing the shear splitting orientation measurements, null measurements, and surface deformation fields for station A005. Fast polarization orientations are shown in black bars, back azimuthal orientations for null measurements in red lines. Left-lateral maximum shear orientation, right-lateral maximum shear orientation, and maximum extension orientation are represented by blue, green, and yellow lines, respectively.

[24] Stations in central northern Tibet located on the Qiangtang and Songpan-Ganzi terranes (stations C004, C009, C010, C011, D008, D009, D019) show fast polarization orientations sub-parallel to the left-lateral maximum shear orientation (Figure 8). The largest delay times, up to 2.2 s, measured on these blocks are for stations C010, C004, KF66A, KF71A and KF76A, (Figures 8 and 11). Estimations of the lithospheric thickness beneath this part of northern Tibet are about 160 km [Kumar *et al.*, 2006], whereas the Moho depth is at ~ 70 km [Sun *et al.*, 2008] and the anisotropic layer has a thickness of approximately 248 km (Table 5). For a 90 km thick continental mantle lithosphere and a typical shear wave velocity of 4.5 km/sec, an 11% anisotropy would be needed to account for the 2.2 s delay time. Since such a high concentration of anisotropy seems unlikely, the contribution to anisotropy from asthenosphere is required.

[25] NW-SE oriented fast polarization orientations are found for stations in the Gansu sub-array (GS01, GS04, GS05, GS07, GS12, GS14, GS16), which are in good agreement with the left-lateral maximum shear orientations (Figure 9). These stations have similar splitting parameters as other stations in eastern Tibet. An averaged delay time of 1.1 s is found for the stations in this region, under similar assumptions for anisotropic strength and upper mantle shear velocity (Table 5), implies an anisotropic layer of 124 km. Since the crust has a thickness of about 50 km in this region [Sun *et al.*, 2008] and the lithosphere is thin, no more than 120 km thick [Zhang *et al.*, 2011], anisotropy from asthenosphere (about 50 km) is required to account the observed delay time. Anisotropy in the asthenosphere for northeastern Tibet could arise from flow generated by continental collision as the lithospheric blocks glide eastward over the asthenosphere. Alternatively, the eastward flow of the asthenosphere would be an effect of the asthenospheric mantle being squeezed between the underthrusting Indian continental lithosphere and the thick lithospheres of the Tarim and Qaidam basin.

[26] Three stations in the southeastern Gansu sub-array (GS09, GS11, and GS18) (Figure 9) were deployed on a mobile corridor connecting two strong cratons, the Sichuan basin (a part of the South China Craton) to the south and the Ordos block (a part of the North China Craton) to the north. Fast polarization orientations of these stations are oriented NW-SE to E-W but do not correlate with strikes of local faults. A large delay time, ~ 2.1 s, is observed at station GS09; this implies a thick anisotropic mantle layer of about 236 km (Table 5). The asthenosphere flows into the channel that lies between the Ordos and Sichuan blocks could arise from asthenospheric flow from eastern Tibet toward eastern China [Zhang *et al.*, 2011]. Such a flow would produce E-W oriented anisotropic fabrics. Our seismic anisotropy observation of this region is similar to the anisotropic long-period Rayleigh wave tomography images, which also found an E-W oriented fast polarization orientation [Zhang *et al.*, 2011].

[27] Although a number of high quality core phase recordings were registered for the stations deployed on the Qaidam basin, a number of measurements were null measurements. Null measurements could be indicative of no anisotropy; however no splitting may also occur if the symmetry axis is vertical or if the polarization of the S-wave is in the fast or slow orientations before entering the anisotropic layer. Another possible interpretation of null measurements arises for regions of very small anisotropy (typically less than 0.4 s) where the resolution of the method is not enough for characterizing it. The large number of null measurements at the stations deployed on the Qaidam basin, limited range of azimuthal distribution of core phases, as well as the apparent small delay times for resolvable event-station pairs, suggest a complex anisotropy where two or more layers could be present. Figure 14 shows the results for station A005 in a rose diagram. The back azimuths directions for null measurements (red bars) show little correlation with the surficial deformation fields (the left-lateral maximum shear orientation in blue, the right-lateral maximum shear extension in green,

and the maximum extension orientation in yellow). However, the resolvable measurements (black bars), in a range from 0° to 30°, show some correlation with the left-lateral maximum shear orientation. This rules out the possibility of a region with no anisotropy. However, the very limited azimuthal coverage for resolvable measurements prevents us from assessing the validity of a multilayered anisotropic model.

7. Conclusions

[28] A comparison of the INDEPTH-IV and previously published shear wave splitting measurements for the entire eastern Tibet and adjacent regions [McNamara *et al.*, 1994; Hirn *et al.*, 1995; Sandvol *et al.*, 1997; Huang *et al.*, 2000; Lev *et al.*, 2006; Sol *et al.*, 2007; Wang *et al.*, 2008] with the best fit left-lateral or right-lateral maximum shear orientations, maximum extension is presented in Figure 13. In regions between the Indus-Yalung Suture and Kunlun faults, the fast orientations of split SKS wave tend to follow the major geological features and the strain field with respect to Eurasia derived from GPS. A clear curved pattern of the fast polarization orientations in southeast Tibet, (92°–100° longitude and 27°–32° latitude) is observed. These anisotropy measurements are interpreted as due to lateral transport of lithospheric and asthenospheric mantle along a curved path that is approximately centered at the apex of the Eastern Himalayan Syntaxis. The clockwise rotation of strike-slip faults and intervening blocks were proposed due to a north-trending right-lateral mega shear in eastern Tibet [England and Molnar, 1990]. The east-striking, southeast-striking and south-striking left lateral faults would then be the response of clock-wise block rotation and shearing would align the mantle fabrics and hence produce the observed seismic anisotropy. Block rotation model would predict that the center of the rotating block would have near zero motion and null anisotropy. However, the observed pattern of seismic fast polarization orientations in eastern Tibet is rather continuous and thus we favor the continuum model for the deformation of the eastern Tibet. A toroidal flow around the open northern edge of the rollback Burma slab could also contribute toward the curved anisotropy pattern in the Eastern Himalayan Syntaxis, but not in northeastern Tibet. At about 105°E longitude and 27°–32°N latitude, in Yunnan province (on the western edge of the Sichuan basin), fast polarization orientations for stations within the fault blocks are not correlated with the local faulting. Since the maximum extension orientation in this region is approximately in the direction of the fast polarizations, it has been suggested [Wang *et al.*, 2008] that this behavior corresponds to a change in deformation regime, from simple shear to pure shear. Since the lithosphere of Sichuan basin is rather thick, fossil anisotropy could play some role in the observed anisotropy. Moreover, the South China is moving SE, independent of the India-Eurasia collision, and hence the traction over the asthenosphere would generate significant anisotropy in the asthenospheric channel. We favor the last interpretation for the observed NW-SE fast polarization orientations for stations on or near the Sichuan basin.

[29] South of 27°N the fast polarization orientation is oriented E-W reflecting the finite strain generated by the back arc poloidal flow of the foundering (roll back) Burma slab.

Stations in the eastern Gansu sub-array lie between two tectonically strong units where the lithosphere is thinner than in the adjacent blocks. The seismic fast orientations measured at these stations are oriented E-W. Large delay times of split core phases indicate that the depth of seismic anisotropy in eastern Tibet, and particularly in northeastern Tibet, extends into the asthenosphere. We suggest that the asthenosphere mantle is “extruded” eastward into this asthenosphere channel that lies between the Ordos plateau and Sichuan Basin [Zhang *et al.*, 2011]. Coherence between the fast polarization orientations measured on the high plateau and left-lateral maximum shear suggest that, at large scale, eastern Tibet deforms in a vertically coherent regime. Qaidam basin, with an elevation of about 3 km, presents a complex anisotropy pattern and the anisotropy parameters could present a different deformation regime than the rest of the higher elevated eastern Tibetan plateau that could be influenced by boundary conditions dictated by the adjacent Tarim basin and Qilian Shan.

[30] The nearly continuous surface velocity field [Zhang *et al.*, 2004], fast polarization directions from crustal azimuthal anisotropy measurements (Y. Yang, personal communication, 2010) and fast polarization orientations from split core phases strongly resemble the flow pattern of a viscous material moving away and around the Eastern Himalayan Syntaxis. The bending of the lithosphere to form the orocline by the underthrusting of Indian continental lithosphere beneath southern central Tibet and foundering Burma slab and subsequent transport of the crust through the orocline would result in crustal thickening within the Eastern Himalayan Syntaxis.

Appendix A: Estimation of Misfit

[31] We seek to test if the fast polarization orientations are consistent with surface deformation fields. Specifically this means testing if the means of two sets of directional data are the same; our procedure uses a circular F test, and is analogous to the F test for linear data [Trauth, 2007].

[32] For a set of N directional data of unit length, θ_i , $i = 1, \dots, N$, the resultant vector, $R = (x, y)$, is defined as the vector average of all the directional data. This is computed by summing its components

$$x = \sum_{i=1}^N \sin \theta_i$$

and

$$y = \sum_{i=1}^N \cos \theta_i$$

[33] The mean resultant length is determined by

$$R = \frac{\sqrt{x^2 + y^2}}{N}$$

[34] And

$$\theta = \arctan(x, y)$$

where the arctangent function covers all four quadrants depending on the signs of x and y . For random directions, R will be near zero, and for nearly unidirectional data R will be near one. The function $1-R$ is often referred to as the circular covariance.

[35] A circular analog of the normal distribution is the Von Mises distribution

$$f(\theta) = \frac{1}{2\pi I_0(\kappa)} e^{\kappa \cos(\theta-\mu)}$$

where $I_0(\kappa)$ is the modified Bessel function of the first kind, μ is the mean direction, and κ is referred to as the concentration parameter. The concentration parameter κ is zero for random directions and large for nearly unidirectional data. For large values, κ approaches $1/(1-R)$ and can be thought of as the inverse of the variance. κ is found by a table look up based on R and n [Gumbel et al., 1953].

[36] As with linear statistics, we can use an F-statistic to test the null hypothesis that the means of two populations are the same. Our circular F-statistic is based on the function

$$F_{1,n-2} = \left(1 + \frac{3}{8\kappa}\right) \frac{(n-2)(R_{SKS} + R_{SFD} - R_T)}{n - R_{SKS} - R_{SFD}}$$

where R_{SKS} , R_{SFD} , R_T are the resultant lengths for the SKS fast polarization orientations, surface deformation field orientations, and the combined data set of polarization and deformation orientations. This F-statistic has 1 degree-of-freedom in the numerator and $n-2$ degrees-of-freedom in the denominator. If F is smaller than the critical value at a certain level of confidence, we can conclude that the two means are statistically the same; if F is larger than such number, we conclude that they are not. We use a 95% confidence level taken from standard F-statistic tables to choose the F critical value.

[37] Circular statistics applies to data ranging from 0 to 360 degrees, while shear wave splitting and deformation data only give values between 0 and 180 degrees. Thus, in order to use circular statistics, we first double all the splitting orientations. We test the null hypothesis for two different regions: the Eastern Himalayan Syntaxis (longitudes 90° – 98° , latitudes 29° – 33°) and northeastern Tibet (longitudes 90° – 108° , latitudes 33° – 36°). Results are show in Tables A1 and A2. For both the Eastern Himalayan Syntaxis and northeastern Tibet the null hypothesis is satisfied at the 95% confidence level only for the left-lateral shear orientations. We conclude that shear wave splitting orientations are consistent with left-lateral shear deformation but not with right-lateral shear or the orientation of elongation.

Table A1. Comparison of Splitting Directions and Deformation Directions for the Eastern Himalayan Syntaxis

	Left-Lateral Direction	Right-Lateral Direction	Elongation Direction
F-value	0.0119	1764.8	43.2156
Critical F-value (95%)	3.9402	3.9402	3.9402

Table A2. Comparison of Splitting Directions and Deformation Directions for Northeastern Tibet

	Left-Lateral Direction	Right-Lateral Direction	Elongation Direction
F-value	0.1960	478.83	114.25
Critical F-value (95%)	3.9258	3.9258	3.9258

[38] **Acknowledgments.** We thank all the members of scientific teams of the INDEPTH-IV passive seismic array and the local residents who helped us during the experiments. Assistance from the Qinghai and Xizang Seismological Bureaus, China Earthquake Administration, for the fieldwork is most appreciated. Discussions with Robert Nowack and Wiki Royden helped with the interpretation of our results. This work is supported by the NSF of China under grants 40520120222 and 40821062, and the U.S. National Science Foundation under grants EAR-0634903 and EAR-0409589.

References

- Argand, E. (1924), La tectonique de l'Asie, *Int. Geol. Congr. Rep. Sess.*, 13, 170–372.
- Babuska, V., and M. Kara (1991), *Seismic Anisotropy in the Earth*, 232 pp., Kluwer Acad., Dordrecht, Netherlands.
- Barrauol, G., and D. Mainprice (1993), A quantitative evaluation of the contribution of crustal rocks to the shear wave splitting of teleseismic SKS waves, *Phys. Earth Planet. Inter.*, 78, 281–300, doi:10.1016/0031-9201(93)90161-2.
- Barrauol, G., M. Bonnin, H. Pedersen, G. H. R. Bokelmann, and C. Tiberi (2011), Belt-parallel mantle flow beneath a halted continental collision: The Western Alps, *Earth Planet. Sci. Lett.*, 302, 429–438, doi:10.1016/j.epsl.2010.12.040.
- Chen, W. P., and S. Özalaybey (1998), Correlation between seismic anisotropy and Bouguer gravity anomalies in Tibet and its implications for lithospheric structures, *Geophys. J. Int.*, 135, 93–101, doi:10.1046/j.1365-246X.1998.00611.x.
- Chen, W. P., M. Martin, T. L. Tseng, R. L. Nowack, S. H. Hung, and B. S. Huang (2010), Shear-wave birefringence and current configuration of converging lithosphere under Tibet, *Earth Planet. Sci. Lett.*, 295, 297–304, doi:10.1016/j.epsl.2010.04.017.
- Civello, S., and L. Margheriti (2004), Toroidal mantle flow around the Calabrian slab (Italy) from SKS splitting, *Geophys. Res. Lett.*, 31, L10601, doi:10.1029/2004GL019607.
- Cowgill, E. (2007), Impact of riser reconstructions on estimation of secular variation in rates of strike-slip faulting: Revisiting the Charchen River site along the Altyn Tagh Fault, NW China, *Earth Planet. Sci. Lett.*, 254, 239–255, doi:10.1016/j.epsl.2006.09.015.
- Davis, P., P. England, and G. Houseman (1997), Comparison of shear wave splitting and finite strain from the India-Asia collision zone, *J. Geophys. Res.*, 102, 27,511–27,522, doi:10.1029/97JB02378.
- England, P., and G. Houseman (1986), Finite strain calculations of continental deformation: 2. Comparison with the India-Asia collision zone, *J. Geophys. Res.*, 91, 3664–3676, doi:10.1029/JB091iB03p03664.
- England, P., and G. Houseman (1989), Extension during continental convergence, with application to the Tibetan plateau, *J. Geophys. Res.*, 94, 17,561–17,579, doi:10.1029/JB094iB12p17561.
- England, P., and P. Molnar (1990), Right-lateral shear and rotation as the explanation for strike-slip faulting in eastern Tibet, *Nature*, 344, 140–142, doi:10.1038/344140a0.
- England, P., and P. Molnar (1997), Active deformation of Asia: From kinematics to dynamics, *Science*, 278, 647–650, doi:10.1126/science.278.5338.647.
- Flesch, L. M., A. J. Haines, and W. E. Holt (2001), Dynamics of the India-Eurasia collision zone, *J. Geophys. Res.*, 106, 16,435–16,460, doi:10.1029/2001JB000208.
- Flesch, L. M., W. E. Holt, P. G. Silver, M. Stephenson, C. Y. Wang, and W. W. Chan (2005), Constraining the extend of crust-mantle coupling in central Asia using GPS, geologic and shear-wave splitting data, *Earth Planet. Sci. Lett.*, 238, 248–268, doi:10.1016/j.epsl.2005.06.023.
- Fu, Y. V., Y. J. Chen, A. Li, S. Zhou, X. Lian, G. Ye, G. Jin, M. Jiang, and J. Ning (2008), Indian mantle corner flow at southern Tibet revealed by shear wave splitting measurements, *Geophys. Res. Lett.*, 35, L02308, doi:10.1029/2007GL031753.
- Gao, S. S., and K. H. Liu (2009), Significant seismic anisotropy beneath the southern Lhasa Terrane, Tibetan Plateau, *Geochem. Geophys. Geosyst.*, 10, Q02008, doi:10.1029/2008GC002227.

- Garzanti, E., and T. Van Haver (1988), The Indus clastics: Forearc basin sedimentation in the Ladakh Himalaya (India), *Sediment. Geol.*, *59*, 237–249, doi:10.1016/0037-0738(88)90078-4.
- Gumbel, E. J., J. A. Greenwood, and D. Durand (1953), The circular normal distribution: Tables and theory, *J. Am. Stat. Assoc.*, *48*, 131–152, doi:10.2307/2280886.
- Haines, A. J., J. A. Jackson, W. E. Holt, and D. C. Agnew (1998), Representing distributed deformation by continuous velocity fields, *Sci. Rep.*, *98/5*, Inst. of Geol. and Nucl. Sci., Wellington, New Zealand.
- Herquel, G., G. Wittlinger, and J. Guilbert (1995), Anisotropy and crustal thickness of northern Tibet: New constraints for tectonic modeling, *Geophys. Res. Lett.*, *22*, 1925–1928, doi:10.1029/95GL01789.
- Hirn, A., et al. (1995), Seismic anisotropy as an indicator of mantle flow beneath Himalayas and Tibet, *Nature*, *375*, 571–574, doi:10.1038/375571a0.
- Holt, W. E. (2000), Correlated crust and mantle strain fields in Tibet, *Geology*, *28*, 67–70, doi:10.1130/0091-7613(2000)28<67:CCAMSF>2.0.CO;2.
- Holt, W. E., N. Chamot-Rooke, X. Le Pichon, and A. J. Haines (2000), The velocity field in Asia inferred from Quaternary fault slip rates and GPS observations, *J. Geophys. Res.*, *105*, 19,185–19,209, doi:10.1029/2000JB900045.
- Huang, W. C., et al. (2000), Seismic polarization anisotropy beneath the central Tibetan Plateau, *J. Geophys. Res.*, *105*, 27,979–27,989, doi:10.1029/2000JB900339.
- Karplus, M. S., W. Zhao, S. L. Klempner, Z. Wu, J. Mechie, D. Shi, L. D. Brown, and C. Chen (2011), Injection of Tibetan crust beneath the south Qaidam Basin: Evidence from INDEPTH IV wide-angle seismic data, *J. Geophys. Res.*, *116*, B07301, doi:10.1029/2010JB007911.
- Kind, R., J. Ni, W. Zhao, W. Wu, X. Yuan, L. Zhao, E. Sandvol, C. Reese, J. Nábělek, and T. Hearn (1996), Evidence from earthquake data for a partially molten crustal layer in southern Tibet, *Nature*, *381*, 1692–1694, doi:10.2307/2890944.
- Kumar, P., X. Yuan, R. Kind, and J. Ni (2006), Imaging the colliding Indian and Asian lithospheric plates beneath Tibet, *J. Geophys. Res.*, *111*, B06308, doi:10.1029/2005JB003930.
- Kumazawa, M., and O. L. Anderson (1969), Elastic moduli, pressure derivatives, and temperature derivatives of single-crystal olivine and single-crystal forsterite, *J. Geophys. Res.*, *74*, 5961–5972, doi:10.1029/JB074i025p05961.
- Lavé, J., J. P. Avouac, R. Lacassin, P. Tapponnier, and J. P. Montagner (1996), Seismic anisotropy beneath Tibet: Evidence for eastward extrusion of the Tibetan lithosphere?, *Earth Planet. Sci. Lett.*, *140*, 83–96, doi:10.1016/0012-821X(96)00045-3.
- León Soto, G., J. F. Ni, S. P. Grand, E. Sandvol, R. W. Valenzuela, M. Guzmán Speziale, J. M. Gómez González, and T. Domínguez Reyes (2009), Mantle flow in the Rivera-Cocos subduction zone, *Geophys. J. Int.*, *179*, 1004–1012, doi:10.1111/j.1365-246X.2009.04352.x.
- Lev, E., M. D. Long, and R. D. van der Hilst (2006), Seismic anisotropy in eastern Tibet from shear wave splitting reveals changes in lithospheric deformation, *Earth Planet. Sci. Lett.*, *251*, 293–304, doi:10.1016/j.epsl.2006.09.018.
- Li, C., R. D. van der Hilst, A. S. Meltzer, and E. R. Engdhal (2008), Subduction of the Indian lithosphere beneath the Tibetan Plateau and Burma, *Earth Planet. Sci. Lett.*, *274*, 157–168, doi:10.1016/j.epsl.2008.07.016.
- Mattauer, M., P. Matte, and J. L. Olivet (1999), A 3D model of the India-Asia collision at plate scale, *C. R. Acad. Sci. Paris*, *328*, 499–508.
- McCaffrey, R., and J. Nábělek (1998), Role of oblique convergence in the active deformation of the Himalayas and southern Tibet plateau, *Geology*, *26*, 691–694, doi:10.1130/0091-7613(1998)026<0691:ROOCIT>2.3.CO;2.
- McKenzie, D. P., and K. F. Priestley (2008), The influence of lithospheric thickness variations on continental evolution, *Lithos*, *102*(1–2), 1–11, doi:10.1016/j.lithos.2007.05.005.
- McNamara, D. E., T. J. Owens, P. G. Silver, and F. T. Wu (1994), Shear wave anisotropy beneath the Tibetan Plateau, *J. Geophys. Res.*, *99*, 13,655–13,665, doi:10.1029/93JB03406.
- Nábělek, J., G. Hetenyi, J. Vergne, S. Sapkota, B. Kafle, M. Jiang, H. Su, J. Chen, B. S. Huang, and the Hi-CLIMB Team (2009), Underplating in the Himalaya-Tibet collision zone revealed by the Hi-CLIMB experiment, *Science*, *325*, 1371–1374, doi:10.1126/science.1167719.
- Najman, Y., et al. (2010), Timing of India-Asia collision: Sedimentological, biostratigraphic, and palaeomagnetic constraints, *J. Geophys. Res.*, *115*, B12416, doi:10.1029/2010JB007673.
- Nelson, K. D., et al. (1996), Partially molten middle crust beneath southern Tibet: Synthesis of Project INDEPTH results, *Science*, *274*, 1684–1688, doi:10.1126/science.274.5293.1684.
- Ni, J., and M. Barazangi (1983), Velocities and propagation characteristics of Pn, Pg, Sn, and Lg seismic waves beneath the Indian Shield, Himalayan Arc, Tibetan Plateau, and surrounding regions: High uppermost mantle velocities and efficient Sn propagation beneath Tibet, *Geophys. J. R. Astron. Soc.*, *72*, 665–689, doi:10.1111/j.1365-246X.1983.tb02826.x.
- Ni, J., and M. Barazangi (1984), Seismotectonics of the Himalayan collision zone: Geometry of the underthrusting Indian plate beneath the Himalayan, *J. Geophys. Res.*, *89*, 1147–1163, doi:10.1029/JB089iB02p01147.
- Ni, J. F., M. Guzman-Speziale, M. Bevis, W. E. Holt, T. C. Wallace, and W. R. Seager (1989), Accretionary tectonics of Burma and the three-dimensional geometry of the Burma subduction zone, *Geology*, *17*, 68–71, doi:10.1130/0091-7613(1989)017<0068:ATOBAT>2.3.CO;2.
- Nicolas, A., F. Boudier, and A. M. Boullier (1973), Mechanisms of flow in naturally and experimentally deformed peridotites, *Am. J. Sci.*, *273*, 853–876, doi:10.2475/ajs.273.10.853.
- Peyton, V., V. Levin, J. Park, M. Brandon, J. Lees, E. Gordeev, and A. Ozerov (2001), Mantle flow at slab edge: Seismic anisotropy in the Kamchatka region, *Geophys. Res. Lett.*, *28*, 379–382, doi:10.1029/2000GL012200.
- Rowley, D. S., and B. S. Currie (2006), Paleo-altimetry of the late Eocene to Miocene sediments from the Lunpola Basin, central Tibet, *Nature*, *439*, 677–681, doi:10.1038/nature04506.
- Royden, L. H., B. C. Burchfiel, R. W. King, Z. Chen, F. Shen, and Y. Liu (1997), Surface deformation and lower crustal flow in eastern Tibet, *Science*, *276*, 788–790, doi:10.1126/science.276.5313.788.
- Royden, L. H., B. C. Burchfiel, and R. D. van der Hilst (2008), The geological evolution of the Tibetan Plateau, *Science*, *321*, 1054–1058, doi:10.1126/science.1155371.
- Sandvol, E., and T. Hearn (1994), Bootstrapping shear wave splitting errors, *Bull. Seismol. Soc. Am.*, *84*, 1971–1978.
- Sandvol E., J. Ni, R. Kind, and W. Zhao (1997), Seismic anisotropy beneath the southern Himalayas-Tibet collision zone, *J. Geophys. Res.*, *102*, 17,813–17,823, doi:10.1029/97JB01424.
- Savage, M. K. (1999), Seismic anisotropy and mantle deformation: What have we learned from shear wave splitting?, *Rev. Geophys.*, *37*, 65–106, doi:10.1029/98RG02075.
- Silver, P. G. (1996), Seismic anisotropy beneath the continents: Probing the depths of geology, *Annu. Rev. Earth Planet. Sci.*, *24*, 385–432, doi:10.1146/annurev.earth.24.1.385.
- Silver, P. G., and W. W. Chan (1991), Shear wave splitting and subcontinental mantle deformation, *J. Geophys. Res.*, *96*, 16,429–16,454, doi:10.1029/91JB00899.
- Sol, S., et al. (2007), Geodynamics of the southeastern Tibetan Plateau from seismic anisotropy and geodesy, *Geology*, *35*, 563–566, doi:10.1130/G23408A.1.
- Sun, Y., M. N. Toksoz, S. Pei, D. Zhao, F. D. Moorgan, and A. Rosca (2008), S wave tomography of the crust and uppermost mantle in China, *J. Geophys. Res.*, *113*, B11307, doi:10.1029/2008JB005836.
- Tapponnier, P., and P. Molnar (1977), Active faulting and tectonics of China, *J. Geophys. Res.*, *82*, 2905–2930, doi:10.1029/JB082i020p02905.
- Tapponnier, P., G. Peltzer, A. Y. Le Dain, R. Armijo, and P. Cobbold (1982), Propagating extrusion tectonics in Asia: New insights from simple experiments with plasticine, *Geology*, *10*, 611–616, doi:10.1130/0091-7613(1982)10<611:PETIAN>2.0.CO;2.
- Tapponnier, P., X. Zhiqin, F. Roger, B. Meyer, N. Arnaud, G. Wittlinger, and Y. Jingsui (2001), Oblique stepwise rise and growth of the Tibet Plateau, *Science*, *294*, 1671–1677, doi:10.1126/science.105978.
- Tilmann, F., J. Ni, and the INDEPTH III Seismic Team (2003), Seismic imaging of the downwelling Indian lithosphere beneath central Tibet, *Science*, *300*, 1424–1427, doi:10.1126/science.1082777.
- Trauth, M. H. (2007), *Matlab Recipes for Earth Science*, 288 pp., Springer, Berlin.
- Tseng, T. L., W. P. Chen, and R. L. Nowack (2009), Northward thinning of Tibetan crust revealed by seismic profiles, *Geophys. Res. Lett.*, *36*, L24304, doi:10.1029/2009GL040457.
- Van der Woerd, J., F. J. Ryerson, P. Tapponnier, Y. Gaudemer, R. Finkel, A. S. Merlaux, M. Caffee, Z. Guoguang, and H. Qunlu (1998), Holocene left-slip rate determined by cosmogenic surface dating on the Xidatan segment of the Kunlun fault (Qinghai, China), *Geology*, *26*, 695–698, doi:10.1130/0091-7613(1998)026<0695:HLSRDB>2.3.CO;2.
- Vinnik, L. P., V. Farra, and B. Romanowicz (1989), Azimuthal anisotropy in the Earth from observations of SKS at Geoscope and NARS broadband stations, *Bull. Seismol. Soc. Am.*, *79*, 1542–1558.
- Wang, C. Y., L. M. Flesch, P. G. Silver, L. J. Chang, and W. W. Chan (2008), Evidence for mechanically coupled lithosphere in central Asia and resulting implications, *Geology*, *36*, 363–366, doi:10.1130/G24450A.1.
- Weeraratne, D. S., S. Karalliyadda, and P. G. Silver (2009), Very little crustal anisotropy in eastern Tibet from regional S phases, the game's over, *Eos Trans. AGU*, *90*(52), Fall Meet. Suppl., Abstract S11A-1690.
- Wolfe, C. J., and P. G. Silver (1998), Seismic anisotropy of oceanic upper mantle: Shear wave splitting methodologies and observations, *J. Geophys. Res.*, *103*, 749–771, doi:10.1029/97JB02023.

- Yao, H., R. D. van der Hilst, and J. P. Montagner (2010), Heterogeneity and anisotropy of the lithosphere of SE Tibet from surface wave array tomography, *J. Geophys. Res.*, *115*, C11018, doi:10.1029/2009JC005788.
- Yin, A., and T. M. Harrison (2000), Geologic evolution of the Himalayan-Tibetan Orogen, *Annu. Rev. Earth Planet. Sci.*, *28*, 211–280, doi:10.1146/annurev.earth.28.1.211.
- Zhang, P. Z., et al. (2004), Continuous deformation of the Tibetan Plateau from global positioning system data, *Geology*, *32*, 809–812, doi:10.1130/G20554.1.
- Zhang, Q., E. Sandvol, J. Ni, Y. Yang, and Y. J. Chen (2011), Rayleigh wave tomography of the northeastern margin of the Tibetan Plateau, *Earth Planet. Sci. Lett.*, *304*, 103–112, doi:10.1016/j.epsl.2011.01.021.
- Zhang, S., and S. Karato (1995), Lattice preferred orientation of olivine aggregates deformed in simple shear, *Nature*, *375*, 774–777, doi:10.1038/375774a0.
- Zhao, J., et al. (2010), The boundary between the Indian and Asian tectonic plates below Tibet, *Proc. Natl. Acad. Sci. U. S. A.*, *107*, 11,229–11,233, doi:10.1073/pnas.1001921107.
- Zhao, W., K. D. Nelson, J. Che, J. Quo, D. Lu, C. Wu, and X. Liu (1993), Deep seismic reflection evidence for continental underthrusting beneath southern Tibet, *Nature*, *366*, 557–559, doi:10.1038/366557a0.